Strength/ductility trade-off of Laser Powder Bed Fusion Ti-6Al-4V: Synergetic effect of alpha-case formation and microstructure evolution upon heat treatments

Quentin Gaillard, X Boulnat, Sophie Cazottes, Sylvain Dancette, Christophe Desrayaud

Strength/ductility trade-off of Laser Powder Bed Fusion Ti-6Al-4V: synergetic effect of alpha-case formation and microstructure evolution upon heat treatments

Quentin Gaillard [a,b], Xavier Boulnat [b,*], Sophie Cazottes [b], Sylvain Dancette [b] Christophe Desrayaud [a]

[a] *Université de Lyon, Mines Saint-Etienne, LGF, UMR CNRS 5307, F-42023 Saint-Etienne, France*

[b] *Université de Lyon, INSA Lyon, MATEIS, UMR CNRS 5510, F-69621 Villeurbanne, France*

∗ *Corresponding author: xavier.boulnat@insa-lyon.fr*

Keywords:

Ti-6Al-4V ; Laser Powder Bed Fusion ; Heat Treatments ; Alpha-case ; Ductility

Abstract

Post-processing heat treatments (HT) are performed on Ti-6Al-4V components fabricated by Laser Powder Bed Fusion (L-PBF) to release the residual stresses and transform the non-equilibrium martensite into a dual-phase $\alpha + \beta$ microstructure. In the present study, post-processing sub-transus HT are conducted at various annealing temperatures for 2 h, with slow cooling either in a larger volumetric horizontal industrial furnace or a smaller volumetric tubular laboratory furnace. These two different furnaces were chosen to significantly modify the atmosphere and generate an oxygen-affected layer on the surface. The results show that the higher the annealing temperature, the coarser the α laths and the higher the β phase fraction. An oxygen-enriched hard and brittle alpha-case layer was revealed only for HT performed in the industrial furnace. The provided data allowed modeling of the oxygen diffusion in Ti-6Al-4V made by L-PBF. It has been found that without the alpha-case, post-processing HT helps to balance the strength/ductility compromise of the alloy in relation to the microstructural evolution. On the other hand, when an alpha-case layer greater than 50 µm is present, the elongation to failure is impacted and decreases as the alpha-case depth increases. Meanwhile, the impact toughness is less affected and remains mainly microstructure-dependent. The loss in ductility was attributed to the presence of cracks that develop at the surface of the samples during tensile solicitation. The opening rate of the crack lips is proportional to the applied strain, and the cracks spread through the brittle alpha-case layer. It has been shown for the first time that the cracks are visible on the sample's surface for stress values lower than half of the material's yield stress. The post-processing HT at 800 °C for 2 h provided a strong and ductile Ti-6Al-4V, which showed a minor effect of the alpha-case on the tensile properties.

1 Introduction

Titanium alloys are widely used in aerospace industry due to their high strength-to-weight ratio and corrosion resistance. Among Ti alloys, ASTM grade 5 Ti-6Al-4V (Ti64) is the most used titanium alloys for aerospace applications [1–3]. Ti64 is a dual-phase $\alpha + \beta$ alloy with excellent mechanical properties and was developed in the 1950s for aircraft structures. It currently holds almost half of the titanium products market share. The manufacturing process of Ti64 components typically involves casting, forging and rolling steps, followed by subsequent machining to obtain the final shape [4, 5]. In recent years, the needs of the aeronautic industry to reduce parts weight, material waste and assembled components have allowed metal additive manufacturing (AM) techniques to be considered a serious alternative to the conventional processes mentioned above [6, 7]. In particular, AM of the Ti64 alloy by Laser Powder Bed Fusion (L-PBF) has gained significant attention for producing complex geometries and high performance components. L-PBF allows for the production of near-net-shape parts and the technique has become mature enough to consider manufacturing structural components for specific applications that require a strong material integrity [7–13]. The L-PBF process is described for example in [6] or [7].

Due to the high thermal gradients generated during the manufacturing of Ti64 through L-PBF, as-built parts are exposed to high tensile residual stresses near the surface [14–17]. These residual stresses can adversely affect the mechanical behavior of the material [18, 19]. Furthermore, due to the high cooling rates involved during the process, as-built L-PBF Ti64 presents an α' martensitic microstructure consisting of fine, hierarchical, and entangled needles [20, 21]. Upon cooling, the α' phase germination is preceded by the formation of columnar β grains with a morphological and crystallographic texture oriented parallel to the building direction [22–25]. The martensitic structure that grows in the parent β grains is typically associated with high mechanical strength but poor ductility [21, 26–30] and limited fatigue properties [31, 32]. To meet the product requirements in terms of static [33] and dynamic mechanical behavior, post-processing operations can be performed on Ti64 components. In particular, post-processing heat treatments (HT) are performed on as-built parts in the sub-transus range to relieve the residual stresses and decompose the martensitic phase into an equilibrium $\alpha + \beta$ mixture, which helps balance the strength / ductility compromise [28–31]. As it is well known that the presence of residual stresses may lead to distortions of the as-built parts after cutting [13, 14, 34], the stress-relieving HT carried out for industrial L-PBF production routines is directly performed on components still attached to their base-plate to ensure the dimensional precision of the parts after removal from the building platform. For components and base-plates of large dimensions, this justifies the need for an atmosphere-controlled industrial furnace equipped with an appropriate volume capable of performing suitable post-processing HT on several L-PBF productions.

When exposed to elevated temperatures in an oxygen-containing environment, titanium and its alloys develop an oxide layer on the surface and an oxygen diffusion zone (ODZ) beneath it [35–37]. Due to the significant oxygen solubility in the α phase of titanium (up to 33 at%) [38],

the presence of higher oxygen contents in $\alpha+\beta$ alloys tends to stabilize the α phase at the expense of the β phase, resulting in the ODZ commonly referred to as "alpha-case" (α-case). Oxygen occupies the interstitial sites of the hexagonal close-packed (HCP) lattice of α titanium and limits the mobility of dislocations [39]. As a result, the alpha-case acts as a hard and brittle layer [40, 41] that degrades the mechanical properties by initiating cracks at the surface under loading [38, 42, 43]. The alpha-case created during high-temperature steps of conventional processes such as casting or forging is typically removed from ingots or semi-products that are machined into performance parts subjected to high static or dynamic loading. However, because the L-PBF products are fabricated near-net-shape, removal of an alpha-case layer generated during post-processing HT involves an additional operation that can be expensive or even impossible for complex geometry parts.

Designing suitable post-processing operations to enhance the mechanical properties of Ti64 alloy fabricated by L-PBF is currently of primary interest for industrial applications. The demonstrated economic viability of this manufacturing process primarily relies on a limited amount and associated cost of required post-treatments [6, 7]. As mentioned above, numerous literature papers focus on the effects of post-processing HT on microstructural and mechanical evolution of Ti64 fabricated by L-PBF. Most of the studies utilized small volume laboratory furnaces, and the vast majority of them tested tensile samples that were machined from rectangular or cylindrical specimens. This means that the observed evolution of mechanical properties is induced by the microstructural evolution only, without taking into account the substantial effects of the surface and sub-surface states, including the possible presence of alpha-case. To date, very few studies have addressed the presence of an alpha-case layer after post-processing HT of Ti64 fabricated by L-PBF [44, 45]. In addition, to our knowledge, the effects of alpha-case layers of different depths on the tensile properties of Ti64 fabricated by L-PBF have not been investigated yet. Consequently, the present study aims to quantify the effects of both microstructural evolution and alpha-case formation during post-L-PBF HT on the static properties of Ti64. To achieve this, batches of samples were heat-treated at various annealing temperatures in an industrial furnace or in a laboratory furnace, which involved different atmospheres and, thus, significant changes in the alpha-case formation. The evolution in terms of microstructure, alpha-case, and static properties is characterized for all batches and compared.

2 Materials and experimental methods

2.1 Material and process

A commercial batch of Ti-6Al-4V (Ti64) pre-alloyed spherical powder, manufactured by Tekna Advanced Materials Inc., Canada, was used. The particles were plasma atomized, and their size distribution ranges from 5 to 25 µm. The chemical composition of the powder batch is detailed in Table 1. All L-PBF samples were built to near-net-shape using a FormUp 350 provided by

AddUp, France. The fabrication took place under an argon (Ar) protective atmosphere without pre-heating of the base plates. The machine is equipped with dual YAG fiber lasers, with a spot size of approximately 70 µm. Each of them was assigned to a specific area of the Ti64 base plate corresponding to the front or back side of the building chamber. Both lasers applied a meander scanning pattern with the scanning direction rotated by 90° between each layer. The process parameters were optimized to obtain near-fully dense parts. Prior to testing, X-ray computed tomography was performed on three vertical tensile specimens with a scan height of 23 mm for the whole specimen width and thickness. A voxel size of 6.5 µm was used and the equivalent diameter of the smallest pores after image analysis was 24 µm, which corresponds to an equivalent volume of 26 voxels. With such parameters, the porosity for each sample is lower than 0.005 % (hence density is higher than 99.995 %, and 99 % of the pores has an equivalent diameter lower than 60 µm. From these results, it is expected that the internal defects play a minor role in the static properties compared to the microstructural evolution [46].
The orientations of the parts are defined in this work in accordance with the ISO/ASTM 52900 standard using the axis of the L-PBF machine, XY being the plane parallel to one deposited layer and Z being the building direction. For each of the six metallurgical conditions studied in this work, a fabrication step was performed to produce a batch including simple geometry samples (cubes, blocks), tensile bars, and Charpy impact specimens. In addition, a final fabrication containing vertical tensile and impact bars, similar to the ones from the six previous batches, was done.

Ti	Al	V	Fe	O	C	N	H
Base	6.22	3.87	0.18	0.14	0.009	0.02	0.004

Table 1: Chemical composition (wt%) of the batch of grade 5 Ti64 powder.

2.2 Post-processing heat treatments (HT)

The first batch of samples will be referred to as the as-built condition thereafter. Parts from the five next batches will be referred to as the Industrial Furnace Heat Treatment (IF-HT) samples. The tensile and impact bars from the supplementary fabrication will be referred to as the Laboratory Furnace Heat Treatment (LF-HT) samples. For every HT performed in this study, an annealing time of 2 h was set to relieve all the internal stresses generated during L-PBF and to ensure a microstructural homogeneity in the entire volume of the thicker components. Following the annealing, a slow cooling rate was employed to allow diffusion of the alloying elements and to obtain a resulting microstructure close to the equilibrium conditions.
Post-processing IF-HT were performed directly after the fabrication step, with the samples still attached to their base plate. The IF-HT were carried out by the Nadcap certified company THERMI-GARONNE (France) in a BMI B84T horizontal gas quenching vacuum furnace. To investigate the effects of annealing temperature on the microstructure and mechanical properties evolution, five temperature values ranging from 720 °C to 980 °C were selected within the

sub-transus domain of the alloy. The Samples' temperature was measured by placing a thermocouple in contact with a Ti64 plate. The corresponding temperature curves for the five IF-HT processes are displayed in Figure 1.a, along with the pressure curves. The IF-HT process involves a preliminary heating above 100 °C for one hour under vacuum to eliminate potential moisture that could penetrate the sample roughness during transportation. Subsequently, the heating chamber is pumped up to a pressure of 1×10^{-4} mbar, and the heating step to the annealing temperature is performed at an average of 10 °C min^{-1}. After completing the annealing time of 2 h, the samples undergo a slow cooling process within the furnace, with the average cooling rate ranging from 1.8 °C min^{-1} for 720 °C IF-HT to 2.8 °C min^{-1} for 980 °C IF-HT. Finally, when the temperature reaches 400 °C, fast cooling is achieved by injecting Ar into the chamber. Post-processing LF-HT were performed on untreated tensile bars and impact specimens that had already been separated from the base plate. LF-HT were carried out in a Nabertherm RHTC 80-450/15 tubular vacuum furnace. The LF-HT cycles were designed with the same temperature/time combinations. Temperature was measured with a type-S thermocouple placed nearby the samples, and the corresponding temperature curves are available in Figure 1.b. No preliminary heating above 100 °C was made, but the samples were cleaned with an ultrasonic device before LF-HT. After pumping the heating chamber up to a pressure of 1×10^{-2} mbar, a heating step is performed at an average of 10 °C min^{-1}, followed by 2 h at the annealing temperature, and then slow cooling in the furnace. The average cooling rate ranges from 4.1 °C min^{-1} for 720 °C LF-HT to 4.7 °C min^{-1} for 980 °C LF-HT. At 400 °C, the sample is removed from the furnace and water-quenched.

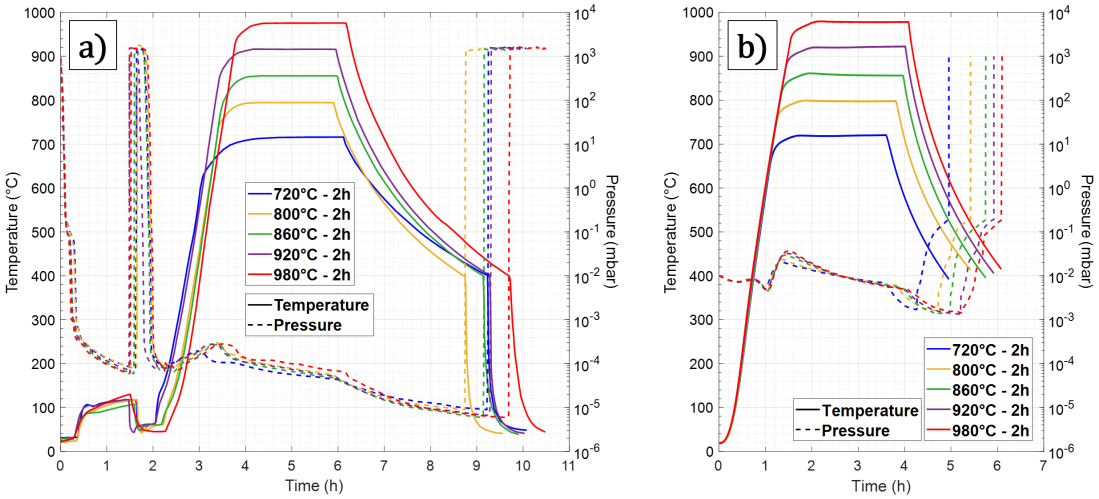

Figure 1: Temperature-pressure curves of (a) Industrial Furnace Heat Treatments (IF-HT) and (b) Laboratory Furnace Heat Treatments (LF-HT).

Following the fabrication for the as-built condition or after IF-HT, samples were separated from the base plates by wire electro-discharge machining (EDM). This step resulted in minor distortions for as-built parts with smallest thicknesses, but it should be noted that no distortions were measured on the HT parts. In fact, it was shown in a previous study that an HT performed for 2 h at 720 °C allows relieving all the internal stresses generated during the fabrication [13].

2.3 Microstructural characterization

The microstructural characterization was conducted by Optical Microscopy (OM), X-ray Diffraction (XRD), and Scanning Electron Microscopy (SEM). Thin slices of material, cut on horizontal XY or vertical YZ cross-sections of 15 mm^3 cubes at about 1 mm from the external surface, were used. All the samples for microstructure examination were ground with 320 grit size SiC paper followed by 9 µm diamond solution. They were then chemically and mechanically polished with a mixture of 50 nm colloidal silica suspension, hydrogen peroxide, and ammonia. Samples used for imaging the microstructure using Back-Scattered Electron (BSE) SEM mode were vibratory polished with colloidal silica. Samples for XRD and Electron Back-Scattered Diffraction (EBSD) were electropolished for 15 s with a solution consisting of perchloric acid, ethanol and 2-butoxyethanol. OM pictures of IF-HT and LF-HT samples were taken with an Olympus GX51 light microscope on the YZ plane of the grip section of tensile bars. The microstructure was revealed by Kroll reagent etching.

Phase analysis by XRD was performed using a Malvern Panalytical X'Pert Pro MRD eqquiped with a Cu-K_α ($\lambda = 1.54$ Å) line focus X-ray source. The diffractometer operated at 45 kV with a tube current of 40 mA, and each scan covered 2θ from 30° to 130° with a step size of 0.04°. It should be noted that due to the presence of crystallographic texture in the samples, XRD scans were conducted for qualitative comparison rather than quantitative evaluation.

Surface phase fractions were determined from BSE images acquired using a ZEISS Supra 55 VP FEG-SEM. Image analysis was performed with ImageJ software to distinguish both phases based on the contrast obtained. The calculated surface fraction represents the average of 20 images taken in the YZ plane for each condition. Additionally, the SEM was used to capture secondary electrons (SE) images of the fracture surfaces of the tensile bars. EBSD was performed on the same SEM operating at 20 kV with an Oxford Instruments Symmetry camera. EBSD maps with different sizes were recorded on the YZ plane for each condition, with a pixel size ranging from 50 nm (as-built) to 150 nm (980 °C - 2 h). EBSD data were treated with the MTEX toolbox [47] on MATLAB software, and α laths boundaries were detected with a 5° misorientation threshold between grains. Grains smaller than 10 pixels were removed from the grain maps, and the thicknesses of the resulting α laths population were determined using the semi-minor axis after ellipse-fitting. Increasing map sizes (and corresponding pixel sizes) with increasing HT temperatures allowed for obtaining the same order of magnitude of grain populations for each condition, enabling a representative comparison of the evolution of the alpha lath sizes.

The alpha-case layer was revealed on samples polished in the XY plane of cubes using Weck reagent etching (ammonium bifluoride dissolved into ethanol and water) for approximately 30 s. Micrographs of the etched samples were captured with an Olympus GX51 light microscope. The alpha-case thickness was quantitatively measured using ImageJ software by analyzing 20 images taken along the entire perimeter of a cube.

2.4 Mechanical characterization

Tensile tests were performed for each condition on dog-bone-shaped specimens that were fabricated with dimensions of 35 mm (gauge length), 7 mm (width), and 3 mm (thickness). These bars were built vertically. Therefore, the tensile load was applied parallel to the building direction Z. Three tensile samples were tested for the as-built, IF-HT and LF-HT conditions. The tensile tests were conducted at room temperature using an Instron Model 1186 tensile system with a cross-head displacement rate fixed at 0.525 mm min^{-1}, resulting in a strain rate of $1.5{\times}10^{-2}$ min^{-1}, in accordance with the NF EN ISO 6892-1 standard. A strain gauge extensometer was employed for accurate strain measurement. The mechanical properties including yield stress at 0.2 % plastic deformation (σ_y), Ultimate Tensile Strength (σ_u), and elongation to failure (ε_f) were obtained as the average of three tests for each condition.

To assess the impact toughness of the material, Charpy impact tests were conducted on standard V-notch specimens fabricated vertically (impact direction orthogonal to Z) using an Amsler Prüfsysteme impact testing machine. The absorbed energy (KV) represents the average value of 5 specimens tested for the as-built, LF-HT and IF-HT conditions.

Vickers microhardness was measured on thin XY polished samples in the as-built, IF-HT and LF-HT conditions using a Buehler microhardness tester with a 1 kg load and an indentation time of 15 s. Indents were made at random locations on the sample's surface, and the reported value is the average of 20 measurements. Additionally, microhardness profiles were obtained from the sample's surface using an applied load of 100 g. The profiles were taken with a staggered arrangement to achieve a spatial resolution of 12.5 µm between each measurement.

To investigate the formation and growth kinetics of strain-induced cracks in the alpha-case layer, *in situ* tensile tests were conducted inside the chamber of the ZEISS Supra 55 VP SEM using the secondary electron imaging mode. As shown in Figure 2, vertical flat tensile samples were cut using wire EDM from a block that had undergone IF-HT at 860 °C for 2 h. The tensile bars were cut at the edge of the block to preserve the alpha-case layer formed in the sub-surface. The samples were 35 mm long and the gauge dimensions were $8 \times 1 \times 1$ mm^3. Tensile tests were performed at a displacement rate of 0.1 mm min^{-1} using a Deben Microtest 2000E Series tensile module placed inside the SEM chamber. The first test involved gradually increasing the applied load, with pauses every 100 N (an average of 115 MPa) to closely observe the gauge surface and detect any visible cracks. In the second test, an already formed crack was monitored to examine its growth kinetics during the tensile test.

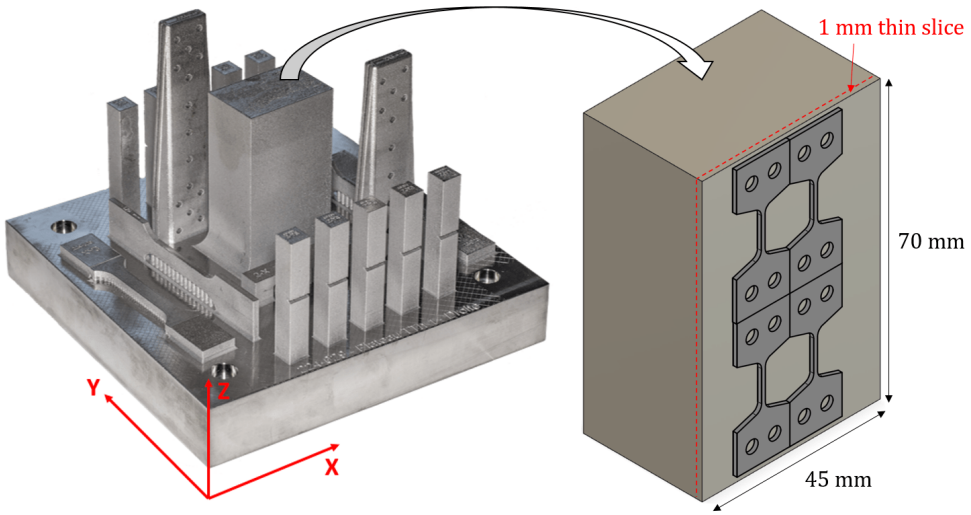

Figure 2: Representative sketch illustrating the location where the samples used for *in situ* tensile tests were cut by wire EDM in the block after IF-HT at 860 °C for 2 h.

3 Results

3.1 Microstructural characterizations

Figure 3 shows cross-sections taken in the YZ plane for the as-built condition and after IF-HT at different annealing temperatures. The micrograph in the as-built condition reveals that the microstructure consists of long columnar prior β grains whose morphological orientation is parallel to the Z-axis. The formation of the β phase at high temperature is driven by the thermal gradients along the building direction, and it grows in epitaxy across the deposited layers [48]. Inside the prior β grains, very fine α' martensite needles are formed during cooling from the β domain due to the process's high cooling rates [20, 49]. With an increase in HT temperature, gradual changes occur: for HT at 720 °C and 800 °C, only slight microstructural modifications are visible at this scale, whereas for HT higher than 860 °C, the presence of lamellar α phase is highlighted. HT at 920 °C and 980 °C lead to a coarse microstructure with the detected presence of globular α phase packets. It should also be noted that for all metallurgical states after HT, the prior β grain structure is conserved, as all the annealing temperatures were chosen below the transus temperature of the alloy. Microstructures obtained after LF-HT were also analyzed, and the same observations are depicted.

Figure 4 presents the Vickers hardness under 1 kg load (HV_{1kg}) measured in the bulk of the material for the as-built condition and after post-processing HT. Both IF-HT and LF-HT show a similar decreasing trend, with hardness values decreasing from 422.2±3.1 in the as-built state to 339.4±4.6 after IF-HT at 980 °C. Slightly higher hardness is measured for LF-HT with increasing temperature. However, hardness values between identical IF-HT and LF-HT conditions are close, suggesting similar microstructures in terms of phase fractions and grain growth.

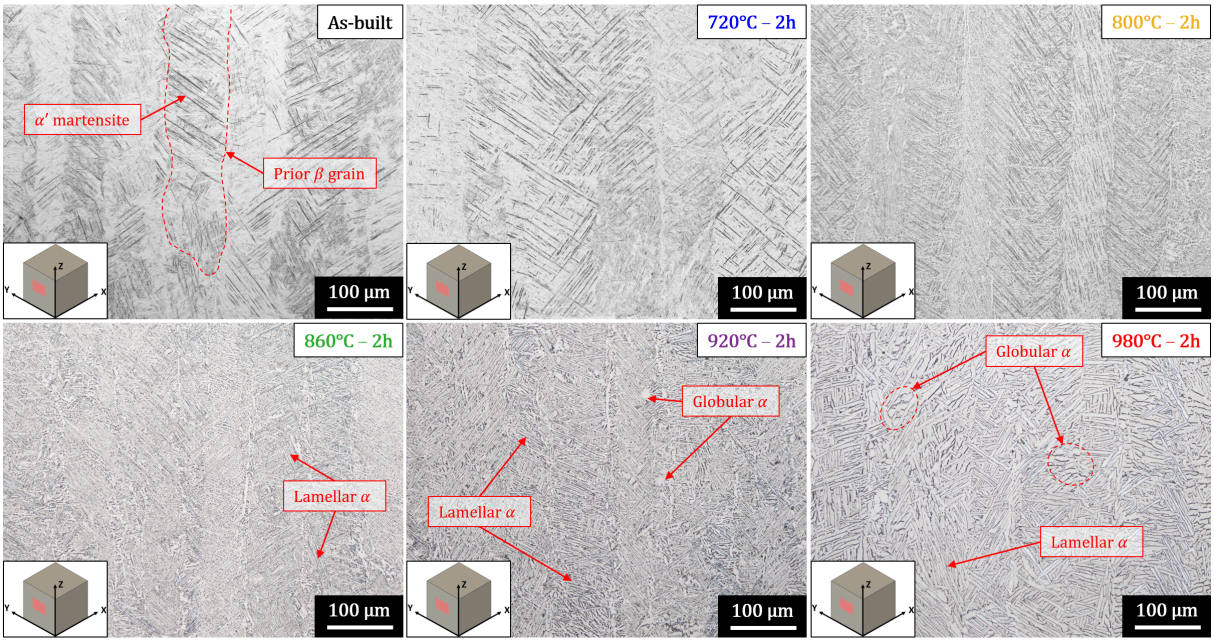

Figure 3: Optical microscope micrographs taken in the YZ plane of L-PBF fabricated Ti64 in its as-built condition and after various sub-transus IF-HT.

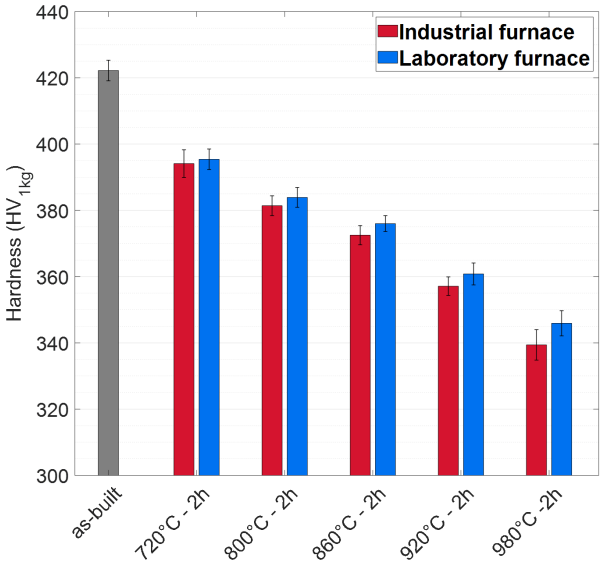

Figure 4: Evolution of hardness (HV_{1kg}) of L-PBF fabricated Ti64 in the as-built condition and after various sub-transus IF-HT and LF-HT.

In order to investigate and quantify the microstructural evolution from the as-built α' state (i.e. grain size and phase fraction), XRD spectra, BSE images, and EBSD orientation maps were obtained as shown in Figures 5, 6, and 7, respectively. XRD spectra and SEM pictures (BSE, EBSD) are presented for as-built and IF-HT conditions only, as they are assumed to be representative of the LF-HT microstructures as well. However, quantitative measurements (α laths thickness, β phase fraction) for the as-built, IF-HT, and LF-HT microstructures are provided in this study.

The XRD spectra displayed in Figure 5.a show that all the peaks in the as-built condition are attributed to α' martensite. After HT, peaks corresponding to the body-centered cubic β phase are detected at all five temperatures. As shown in Figure 5.b, the β (110) peak around 40° exhibits an increase in intensity with increasing HT temperature, indicating a higher β phase fraction. Additionally, the β (110) peak position is shifted to lower 2θ angles with increasing temperatures. Despite these changes, the α phase remains the dominant fraction for all conditions, as the α peaks are significantly more intense than the β ones. Moreover, the full width at half maximum (FWHM) of the α' peaks in the as-built condition is larger than that of the α'/α peaks after HT. The presence of residual stresses is associated with a high dislocation density, and therefore, a high stored energy that affects the shape of the diffraction peak [50]. Internal stress relaxation during HT leads to thinner peaks [51].

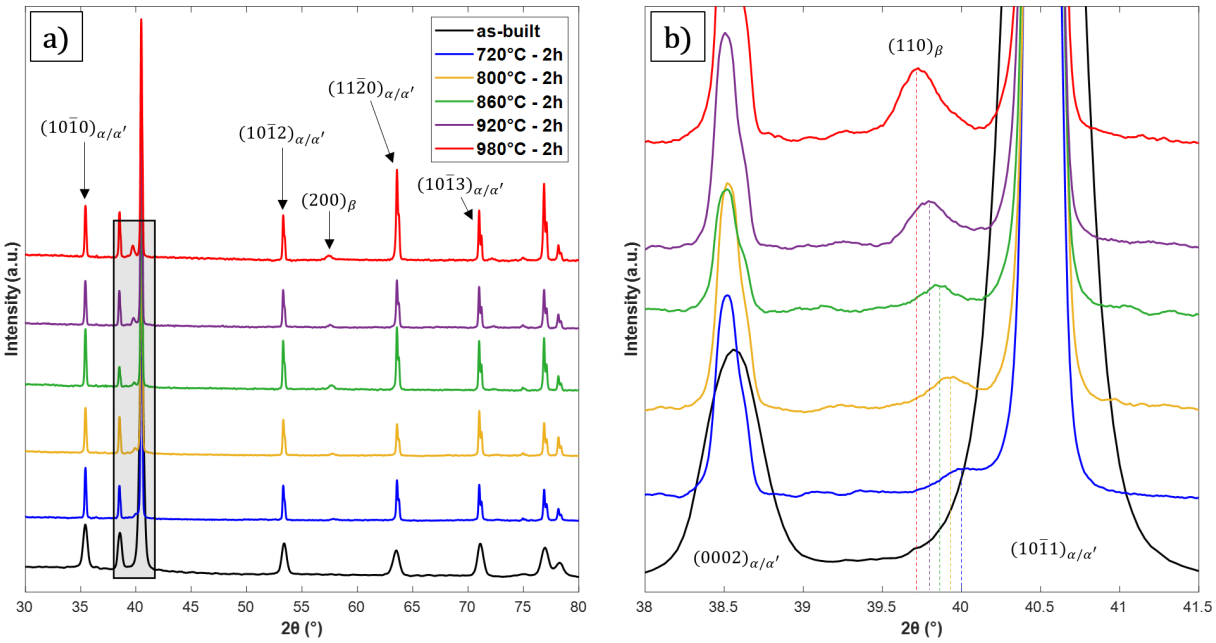

Figure 5: (a) X-ray diffraction (XRD) spectra of L-PBF fabricated Ti64 in the as-built condition and after various sub-transus IF-HT and (b) magnified view of the β (110) peak around 40°.

The α/β phases fraction evolution was estimated from SEM-BSE micrographs, similar to the ones presented in Figure 6.a. The entangled microstructure and the needle-like structures of the hexagonal phase are retained for each condition. However, the martensite decomposition results in the redistribution of alloying elements. Specifically, the diffusion of the $\alpha-$forming element aluminium (Al) tends to enrich the α phase, while the diffusion of the $\beta-$forming element vanadium (V) tends to enrich the β phase. The difference in atomic number between alloying elements leads to varying contrast in BSE imaging between the α and β phases [28, 52]. According to the EBSD phase map in Figure 6.b, the β phase nodules (in red) germinate between the α laths (in blue). Hence, the light areas on the BSE pictures are attributed to the β phase, whereas the dark areas are attributed to the α phase. The average apparent β phase fraction of every condition calculated from BSE pictures is presented in Figure 6.c. The

fraction ranges from 2.2±0.3 % for IF-HT at 720 °C to 7.0±0.5 % for IF-HT at 980 °C. The evolution follows the same trend for LF-HT conditions, with only slightly more β phase observed at higher annealing temperatures. It should be noted that this increase in the β phase fraction from 720 °C to 980 °C coincides with the intensity evolution of the β (110) peak in Figure 5.b.

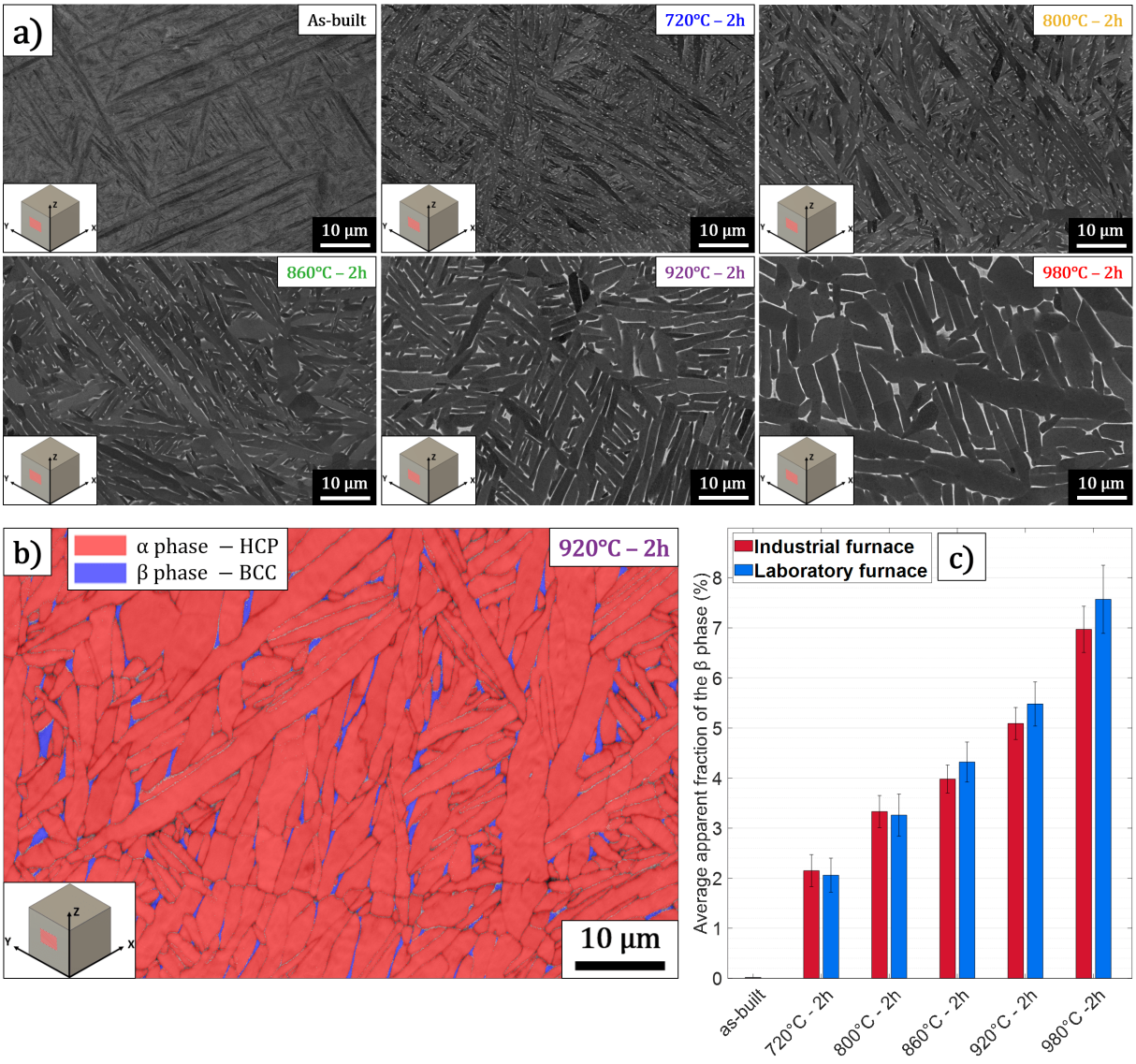

Figure 6: (a) SEM-BSE micrographs of L-PBF fabricated Ti64 in the as-built condition and after various sub-transus IF-HT. (b) EBSD phase map of the specimen subjected to IF-HT at 920 °C for 2 hours. (c) Average apparent fractions of the β phase measured by image analysis from SEM-BSE images.

In Figure 6.a, it becomes evident that the size of both the α and β grains increases with higher annealing temperatures. As the thickness of α laths significantly influences the mechanical response of Ti64 alloy [21, 28, 53, 54], special attention was given to quantifying the evolution of the α laths morphology. To achieve this, α laths were identified from the EBSD orientation maps, as illustrated in Figure 7. During the cooling of the fusion bath in the L-PBF process,

the $\beta \longrightarrow \alpha'$ transformation follows the Burgers Orientation Relationship (BOR) [55], resulting in an acicular microstructure composed of several (up to 12) α' variants within each parent β grain [24, 56]. The presence of numerous ultra-fine α' needles growing in multiple directions with various crystallographic orientations enables the numerical identification of α laths from EBSD maps using a misorientation criterion. In contrast, adjacent α laths grouped in colonies that share the same crystallographic orientation in lamellar Ti64 microstructures are more challenging to distinguish through EBSD orientation maps [53, 57].

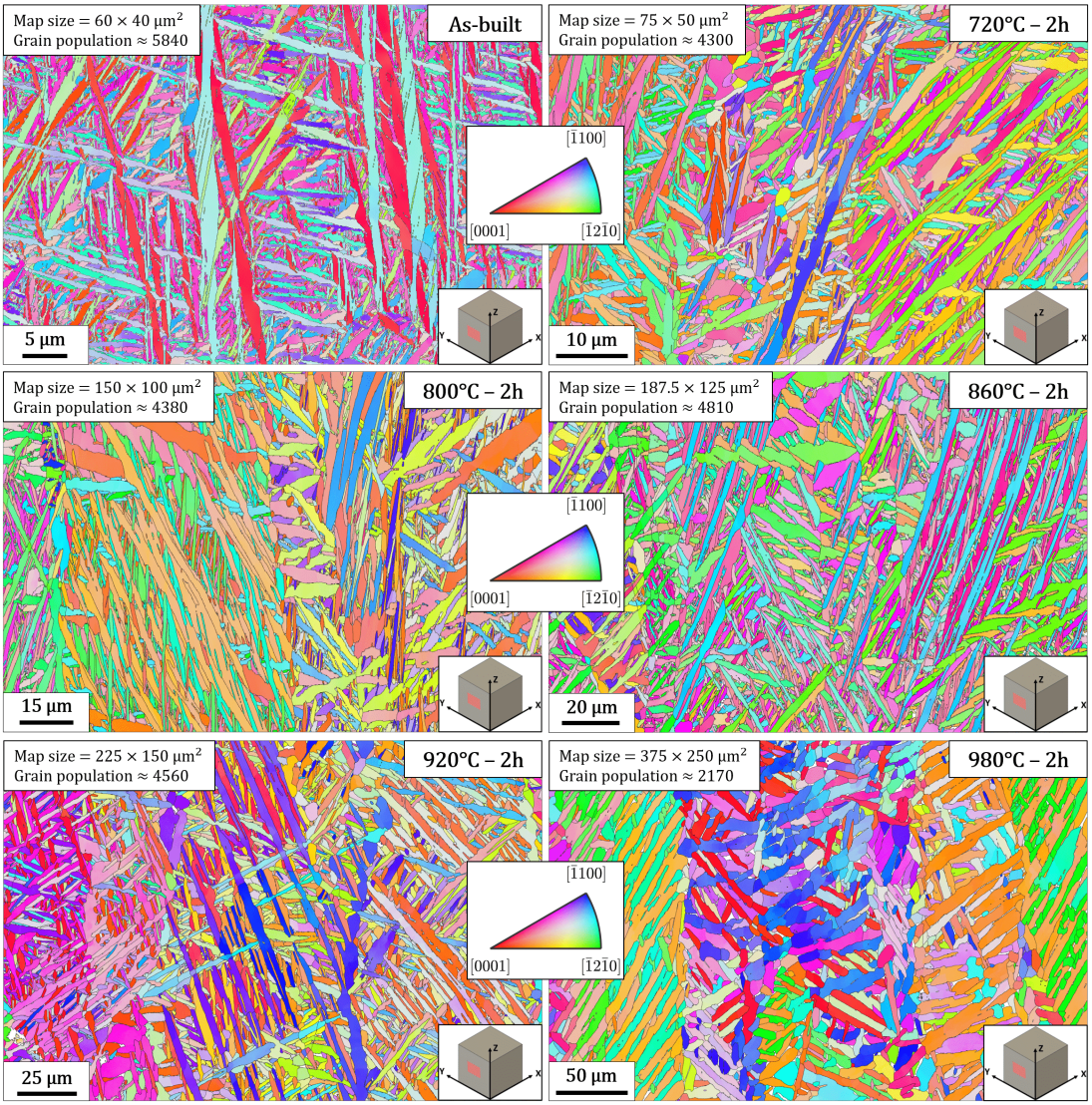

Figure 7: EBSD inverse pole Figure α orientation maps of L-PBF fabricated Ti64 in the as-built condition and after various sub-transus IF-HT. The maps were taken in the YZ plane of a cube, with the build direction Z serving as the reference.

After sub-transus HT, the α' transforms into $\alpha + \beta$ phases, while retaining the same morphological and crystallographic organization of the martensitic structure. Using grain detection on the six EBSD maps acquired in each condition, a grain population containing morphological information (apparent length, apparent thickness) was extracted. The population size converges

to an average of 5840 identified α' needles in the as-built condition, and an average of 2170 identified α grains after IF-HT at 980 °C. Figures 8.a and 8.b display the apparent α laths thickness distributions obtained from the data acquired through grain detection on EBSD maps. The average α laths thickness for each condition is shown in Figure 8.c. The evolution with annealing temperature follows an exponential trend, with the α laths becoming thicker as the temperature approaches the beta transus of the alloy (around 1 000 °C). The values measured using this EBSD method are similar for IF-HT and LF-HT conditions, with only slightly thicker α laths after IF-HT. The values of α laths thickness and β phase fraction measured for the as-built condition and after IF-HT and LF-HT conditions are summarized in Table 2, section 3.3.

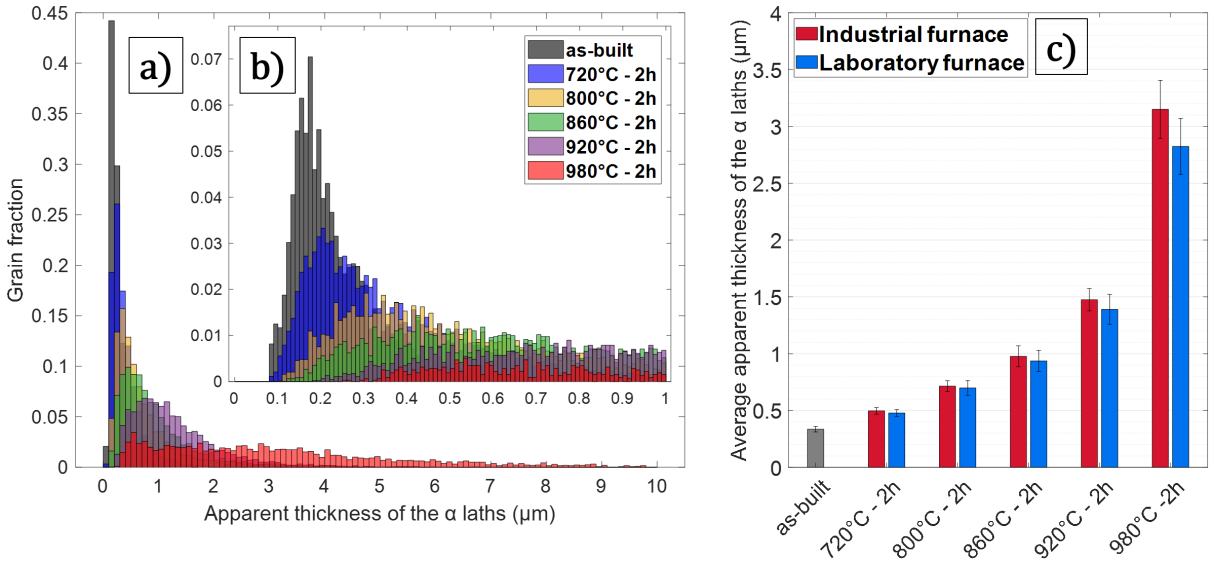

Figure 8: Apparent thickness distribution of the α laths measured from Figure 7 an plotted with a bin width of (a) 0.1 µm, (b) 0.01 µm and (c) average apparent thickness measured for the as-built, IF-HT and LF-HT conditions.

3.2 Alpha-case characterisation

Figure 9.a displays representative micrographs of XY cross-sections taken at the edge of a cube for each IF-HT condition. Figure 9.b exhibits representative micrographs of XY cross-sections taken at the edge of a half tensile specimen before and after LF-HT. Chemical attack with Weck reagent was performed on all the samples to reveal the alpha-case layer, which appears in white. The contrast between the oxygen-enriched material (alpha-case) and the substrate allows for estimating the depth of the alpha-case layer from these pictures. In the as-built state, no presence of alpha-case was found. After IF-HT at 720 °C, a thin 11±1 µm white layer is visible below the surface of the sample. The alpha-case depth increases with the annealing temperature, and the maximum measured thickness for IF-HT at 980 °C is 185±8 µm. The average alpha-case thickness values measured for all IF-HT conditions are reported in Table 2. However, as shown in Figure 9.b for the condition at 980 °C for 2 h, no presence of alpha-case was revealed on the samples after LF-HT.

It is widely acknowledged that the presence of oxygen trapped into the alpha-case layer contributes to an increase in the hardness of titanium alloys through solid solution strengthening [40, 58]. Figure 10 shows microhardness profiles taken from the surface of Ti64 cubes for IF-HT at 860 °C, 920 °C, and 980 °C. For IF-HT at 720 °C and 800 °C, the lateral resolution of 12.5 µm obtained with indents by applying a staggered arrangement was not sufficient to obtain an exploitable profiles. In can be observed that the hardness decreases from the surface, indicating a reduction in oxygen content [40, 41, 58]. The hardness then stabilizes at a constant value close to the bulk hardness reported in Table 2. Using the measured microhardness values and fitting them with an 8^{th}-degree polynomial equation, the profile evolution was modeled. The fitted data lines in Figure 10 show this modeling. Based on these fits, the alpha-case thicknesses were estimated to be 62.5 µm, 112.5 µm, and 212.5 µm for IF-HT at 860 °C, 920 °C, and 980 °C, respectively. These thicknesses were determined at the points farthest from the surface with a hardness value 5 % higher than the bulk hardness. These values are higher than the estimated alpha-case thicknesses obtained from white-layer measurements on etched samples, indicating that oxygen hardening is more sensitive to even small changes in oxygen content, whereas only areas with the highest oxygen concentrations are revealed with chemical attack using Weck reagent. This suggests that examination with optical microscopy alone could lead to an underestimation of the alpha-case depth.

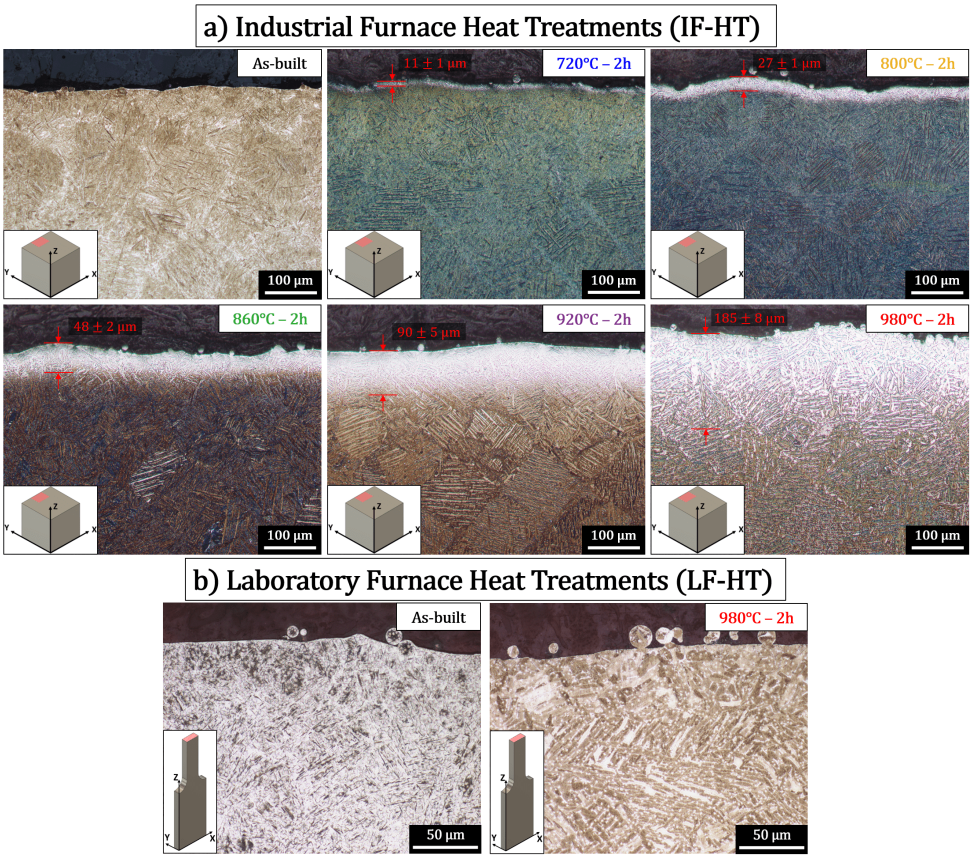

Figure 9: Optical microscope micrographs taken at the edge of cross-sections in the XY plane of (a) cubes before and after various IF-HT conditions, and (b) half tensile specimens before and after LF-HT. These micrographs were subjected to chemical attack with Weck reagent.

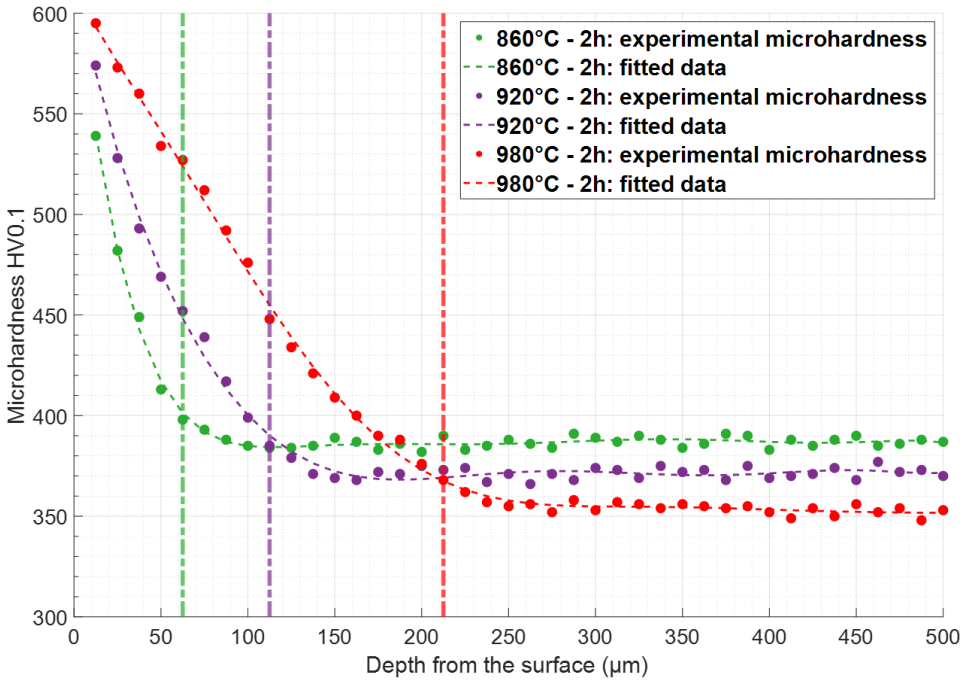

Figure 10: Microhardness (HV0.1) profiles obtained from the surface of Ti64 samples subjected to various sub-transus IF-HT conditions. The vertical dotted lines correspond to the estimated alpha-case depth based on the microhardness profiles.

3.3 Impact and tensile properties

Figure 11.a displays the tensile engineering stress-strain curves of as-built and heat-treated specimens (IF-HT and LF-HT), and the corresponding mechanical properties (σ_y, σ_u and ε_f) are listed in Table 2. In the as-built condition, the tensile properties are characterized by high strength but low ductility, which is typical of the martensitic microstructure of Ti64 fabricated by L-PBF [21, 27, 28, 52, 59, 60]. After HT, both σ_y and σ_u show a similar decreasing trend as the hardness (see Figure 4), gradually decreasing with increasing temperature. σ_u ranges from 1 279±15 MPa in the as-built state to 965±11 MPa after LF-HT at 980 °C, representing a 25 % reduction in tensile strength. Regarding ductility, ε_f is doubled after IF-HT at 720 °C, with a further increase observed after IF-HT at 800 °C. However, for IF-HT at 860 °C and 920 °C, ε_f decreases compared to the previous states, and a more significant drop in ductility is observed for IF-HT at 980 °C. In contrast, LF-HT samples show a superior ε_f for annealing temperatures above 860 °C, with the elongation to failure reaching 18.7±0.7 % for LF-HT at 980 °C, representing a remarkable 450 % gain in ductility compared to the as-built state. This value is also 4.7 times higher than for IF-HT at the same annealing temperature.

The impact energy in the as-built condition is low (4.8±0.2 J); however, after HT at 720 °C, the value doubles comparatively to ε_f. With increasing annealing temperature, KV progressively increases, reaching 15.2±0.6 and 24.8±1.2 after IF-HT and LF-HT at 980 °C, respectively. Despite the scarcity of references on the impact toughness of Ti64 fabricated by L-PBF, the values found is this study are comparable to those reported in references [61–64].

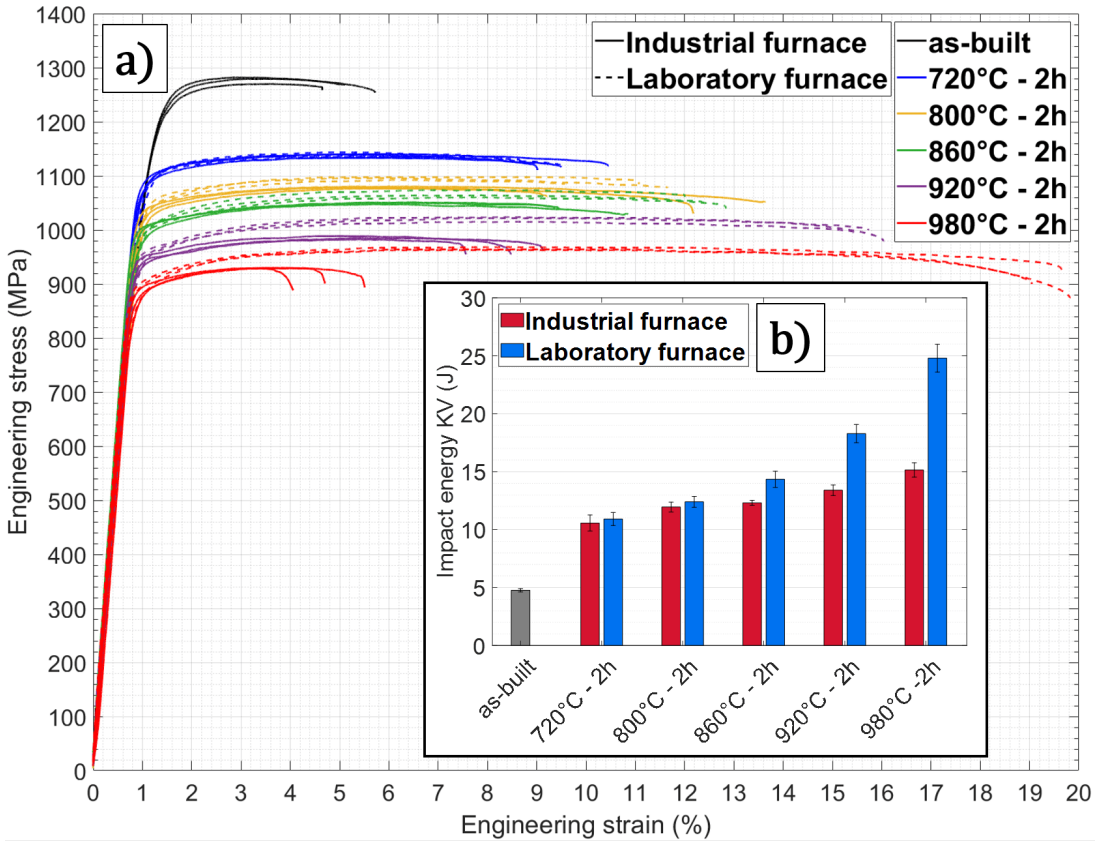

Figure 11: (a) Engineering stress-strain curves of the vertically built IF-HT and LF-HT samples, and (b) measured impact energy of the vertically built IF-HT and LF-HT samples.

Condition	Furnace	α laths thick-ness (µm)	β phase fraction (%)	Alpha-case thick-ness (µm)	HV_{1kg}	σ_y (MPa)	σ_u (MPa)	ε_f (%)	KV (J)
As-built	-	0.34 ± 0.02	0	0	422 ± 3	1 161 ± 25	1 279 ± 15	4.1 ± 0.5	4.8 ± 0.2
720 °C - 2 h	IF	0.50 ± 0.03	2.2 ± 0.3	11 ± 1	394 ± 4	1 087 ± 17	1 138 ± 13	8.7 ± 0.9	10.6 ± 0.7
	LF	0.48 ± 0.03	2.1 ± 0.3	0	395 ± 3	1 089 ± 13	1 138 ± 14	7.8 ± 1.0	10.9 ± 0.6
800 °C - 2 h	IF	0.72 ± 0.05	3.3 ± 0.3	27 ± 1	381 ± 3	1 027 ± 15	1 078 ± 11	10.8 ± 2.6	11.9 ± 0.4
	LF	0.70 ± 0.06	3.3 ± 0.4	0	384 ± 3	1 037 ± 17	1 095 ± 12	9.8 ± 1.8	12.4 ± 0.5
860 °C - 2 h	IF	0.98 ± 0.09	4.0 ± 0.3	48 ± 2	373 ± 3	995 ± 18	1 049 ± 11	9.0 ± 1.0	12.3 ± 0.3
	LF	0.94 ± 0.09	4.3 ± 0.4	0	376 ± 3	990 ± 15	1 066 ± 16	11.5 ± 0.8	14.3 ± 0.7
920 °C - 2 h	IF	1.48 ± 0.10	5.1 ± 0.4	90 ± 5	357 ± 3	936 ± 15	985 ± 10	7.6 ± 0.9	13.4 ± 0.5
	LF	1.39 ± 0.13	5.5 ± 0.5	0	361 ± 3	949 ± 17	1 020 ± 13	14.9 ± 0.7	18.3 ± 0.8
980 °C - 2 h	IF	3.15 ± 0.26	7.0 ± 0.5	185 ± 8	339 ± 5	877 ± 16	929 ± 9	4.0 ± 0.8	15.2 ± 0.6
	LF	2.82 ± 0.25	7.6 ± 0.8	0	346 ± 4	892 ± 14	965 ± 11	18.7 ± 0.7	24.8 ± 1.2

Table 2: Microstructural parameters and mechanical properties of Ti64 fabricated using L-PBF in the as-built condition and after various sub-transus IF-HT and LF-HT processes.

3.4 Oxygen embrittlement and generation of strain-induced cracks

Figure 12 presents SEM-SE pictures taken at the edge of the fracture surface of broken tensile samples after IF-HT at 860 °C, 920 °C, and 980 °C. Each fracture surface shows two distinct zones. Just below the sample's surface, a brittle zone with an interlamellar fracture mode is visible. In contrast, in the bulk of the specimen below the brittle zone, a ductile zone with the presence of dimples is observed. The boundary between the brittle and ductile zones is clearly distinguishable, allowing for the measurement of the brittle zone thickness. The thickness values indicated in Figure 12 represent the average of 10 measurements taken along the perimeter of one specimen for each condition. These values are in close agreement with the alpha-case thicknesses estimated from microhardness profiles (see section 3.2). It is well-known that oxygen can embrittle titanium alloys, leading to a shift from ductile to brittle fracture mode when the oxygen content reaches 0.3 wt% or above [58, 65, 66]. Similarly, a ductile to brittle transition was observed at the edge of the fracture surface of the Charpy impact specimens after IF-HT.

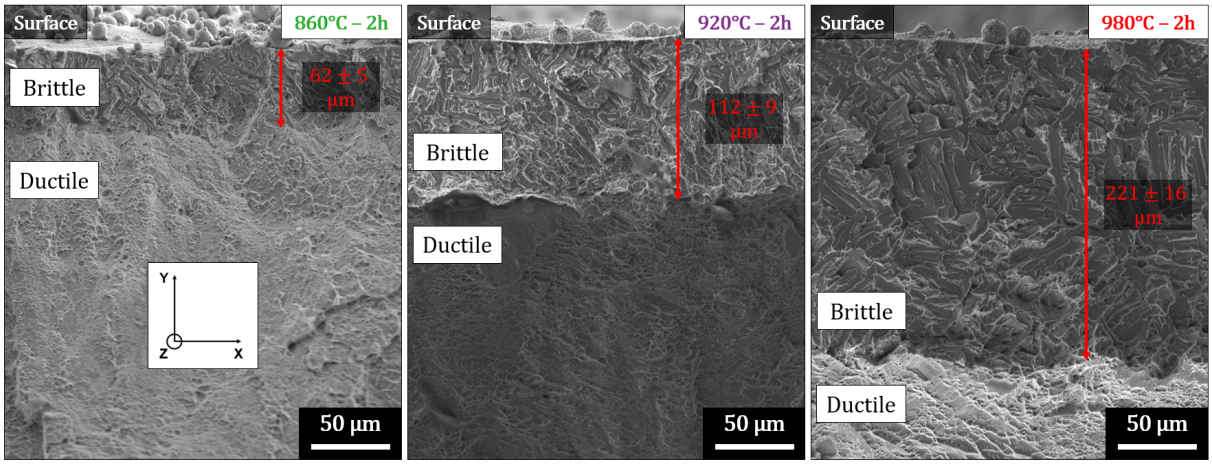

Figure 12: SEM-SE images captured at the edge of the fracture surface of Ti64 tensile specimens subjected to various sub-transus IF-HT.

After the tensile tests, the surface of each half-tensile specimen subjected to IF-HT exhibits a high density of open cracks, homogeneously disseminated along the gauge length of the specimen. As shown in Figure 13.a, these cracks are visible to the naked eye for IF-HT at 920 °C (and thus for IF-HT at 980 °C). Figures 13.b and 13.c show, respectively, a metallographic cross-section of the same specimen before and after chemical attack with Weck reagent. It can be observed that the distance between two consecutive cracks is approximately constant along the gauge length. Moreover, the depth of the cracks is almost equal to the alpha-case thickness, as highlighted after the chemical attack. On the post-mortem specimen, most of the cracks are blunt after crossing the alpha-case (see Figure 13.d). This behavior could be explained by a plastification phenomenon occurring around the curvature of the crack when it enters the ductile zone (see Figure 12).

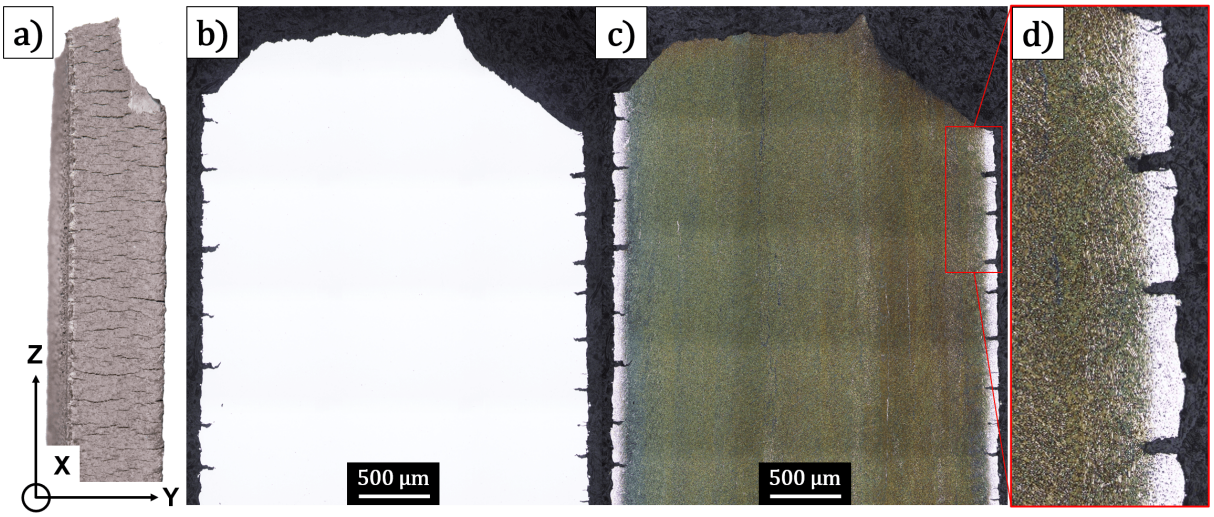

Figure 13: (a) Visualization of cracks on the surface of a post-mortem tensile specimen subjected to IF-HT at 920 °C for 2 hours. Visualization of cracks on a cross-section of the same specimen before (b) and after (c) chemical attack with Weck reagent. (d) Visualization of blunt cracks at the alpha-case boundary.

To investigate the formation and growth kinetics of these cracks, in-situ tensile tests were conducted in the SEM chamber on small specimens cut from the surface of a block after IF-HT at 860 °C (see Figure 2). The examination of the sample's surface under secondary electrons was performed on the oxidized surface, which presented an alpha-case layer around 50 µm deep after IF-HT (see Figure 9 and Table 2). No cracks were visible on the sample's surface before the tests. During the first test, conducted by gradually increasing the applied load, the first cracks were observed at a load of 400 N, corresponding to an average macroscopic stress of of 460 MPa. It should be noted that this stress value is less than half of the yield stress of the material in the metallurgical state obtained after HT at 860 °C for 2 h (see Figure 11 and Table 2). Similarly to the observation mentioned in Figure 13.a, the cracks were uniformly distributed across the observed gauge length surface of the specimen. However, these cracks were barely open and detectable under SEM imaging. Another test was conducted to study the growth and opening kinetics of a crack, from a macroscopic stress of765 MPa until the specimen's failure. Figure 14.a presents the evolution of the crack during the tensile test. The first four pictures were taken in the elastic domain, the fifth picture during the transition from elasticity to plasticity, and the last four pictures were taken in the plastic domain. Figures 14.b and 14.c show respectively the corresponding stress-displacement curve and the distance between the crack lips measured at the middle of the SEM-SE pictures. The dots numbered in Figures 14.b and 14.c correspond to the picture numbers in Figure 14.a. In the elastic domain, the crack remains almost closed, with a very slight increase in the opening value from 765 MPa (dot 1) to 935 MPa (dot 4). Upon transitioning to the plastic domain, the crack starts to open faster, and the growth is mainly located in the plastic domain. The dotted red line plotted in Figure 14.c is a linear approximation calculated between dots 5 to 8. This indicates that in the plastic domain, the crack opening kinetics at the surface is almost constant for a constant displacement rate, leading to a distance between the crack lips proportional to the displacement. This suggests that the

opening kinetics of the cracks are controlled by the applied strain. After failure (dot 9), the crack opening shows a slight decrease that could be explained by the elastic springback of the sample. In a nutshell, the cracks formed in the alpha-case during tensile loading appear in the elastic domain, and their opening is primarily induced by plasticity.

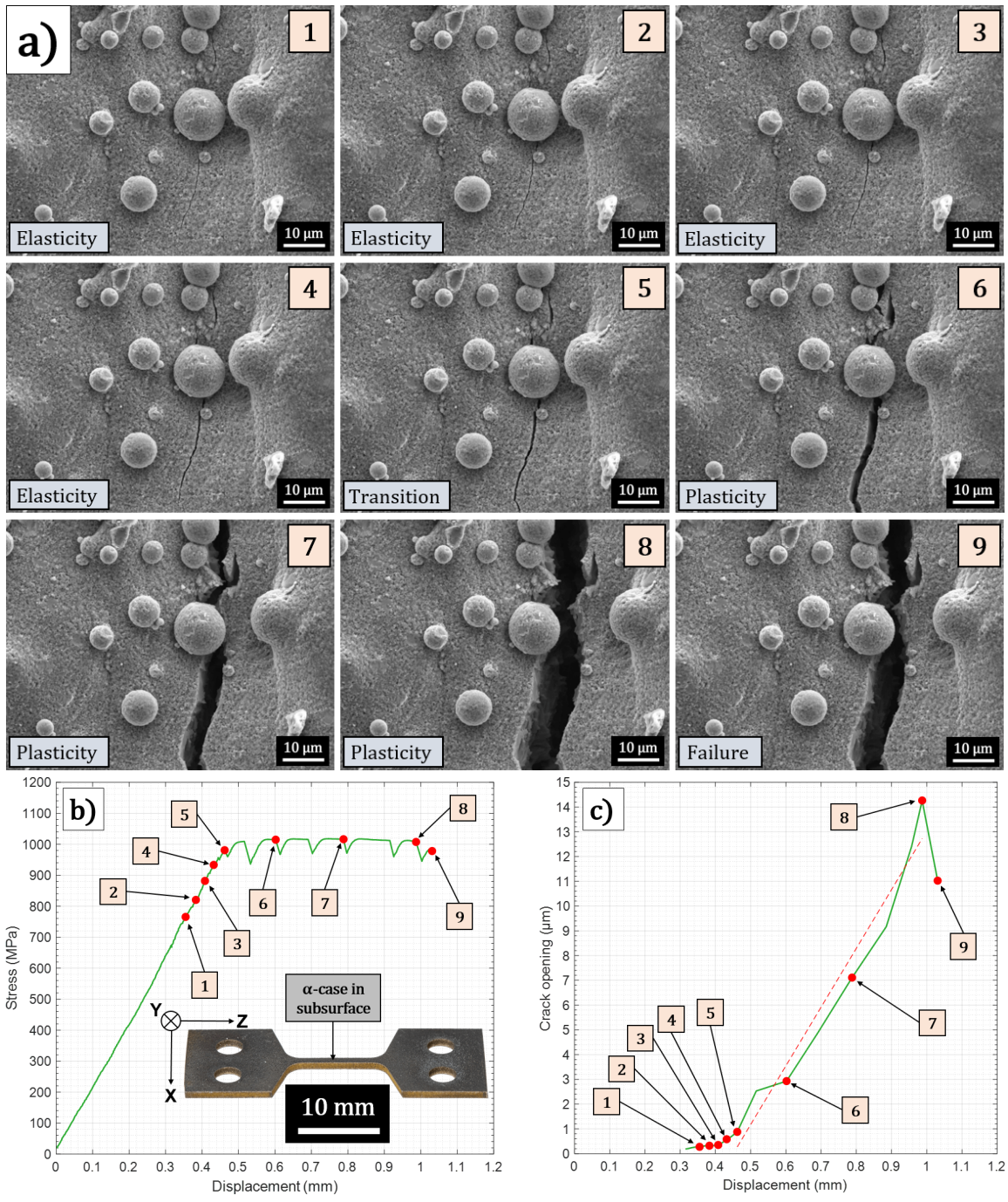

Figure 14: (a) Evolution of a strain-induced crack during an *in situ* tensile test. (b) Corresponding stress-displacement curve obtained from a micro-tensile sample cut in the block after IF-HT at 860 °C for 2 h. (c) Corresponding measurements of the distance between the crack lips taken at the middle of each picture in (a).

4 Discussion

4.1 Role of annealing temperature on microstructural evolution

The microstructure consisting of 100 % entangled martensitic needles within prior β grains, is consistent with observations presented in the literature [7, 25, 28, 67] for the as-built condition. As shown in Figure 7, the as-built condition exhibits highly heterogeneous sizes of the α' needles, with an average α' laths thickness of 0.34±0.02 µm. After post L-PBF HT, the final microstructure strongly depends on the annealing temperature. For all the studied temperatures, martensite decomposition ($\alpha' \longrightarrow \alpha + \beta$) occurs, and β peaks are detected by XRD as presented in Figure 5. As indicated in Figure 15.a, holding the alloy at high temperatures (> 700 °C) leads to an increasing fraction of the β phase at equilibrium, ultimately reaching 100 % of β phase at the transus temperature. Figure 15.b clearly illustrates that the higher the β phase fraction, the closer the alloying element content in β to the nominal content in the alloy (10.50 at% for Al and 3.46 at% for V). During slow furnace cooling, a low fraction of β matrix formed at high annealing temperatures can become stabilized at room temperature (Figure 15.a), resulting in a higher content of the β-stabilizing element V (Figure 15.b). Furthermore, holding the material at higher annealing temperatures followed by a slow cooling rate allows a higher concentration of V to diffuse from the α laths to the β matrix located along the boundaries of the α grains (Figures 6.a and 6.b), leading the material to approach a closer-to-equilibrium state [32, 53, 68]. Consequently, there is an increasing concentration of stabilized and retained β phase fraction at room temperature with increasing annealing temperature, as shown in Figure 5.b and 6.c.
Figure 5.b also indicates that the lattice parameter of the β phase increases with annealing temperature, as evidenced by the shift in the Bragg angle of the β (110) peak towards lower values. This observation aligns with findings from other authors who studied similar sub-transus heat treatments at different annealing temperatures followed by furnace cooling [29, 30]. However, no specific explanation was provided in their work for this particular result. In the β phase, it is known that higher vanadium content leads to a smaller lattice parameter [69, 70], due to the fact that both the substitutional solid solution elements V (0.132 nm) and Al (0.143 nm) have smaller atomic radii than Ti (0.147 nm). Furthermore, for post L-PBF heat treatments with fixed annealing temperatures but increasing holding times, Casadebaigt et al. [58] (HT at 600 °C) and Cao et al. [21] (HT at 800 °C) observed a shift of the β (110) peak towards higher angles, which they attributed to the solute redistribution of Al and V during prolonged annealing. In the present work, the shift towards smaller angles could be attributed to an interface effect between the α and β phases. The BOR [55] governs the crystallographic orientation for both the $\beta \longrightarrow \alpha$ and $\alpha \longrightarrow \beta$ transformations, resulting in a crystallographic correspondence $\{0001\}_\alpha$ // $\{110\}_\beta$ at the α/β interfaces in titanium alloys [71, 72]. To accommodate the small misfit between the *hcp* and the *bcc* structures and enable the formation of a coherent α/β interface, lattice distortions in the β phase have been reported in a metastable β-Ti alloy [73]. The results shown in Figure 6.a indicate that the higher the annealing temperature, the larger the β grains along the α grain boundaries. In the case of thicker β grains, the possible

lattice distortions near the interface may have a lesser impact on the overall lattice structure, which could explain the increase in the lattice parameter obtained by XRD for the β (110) peak.

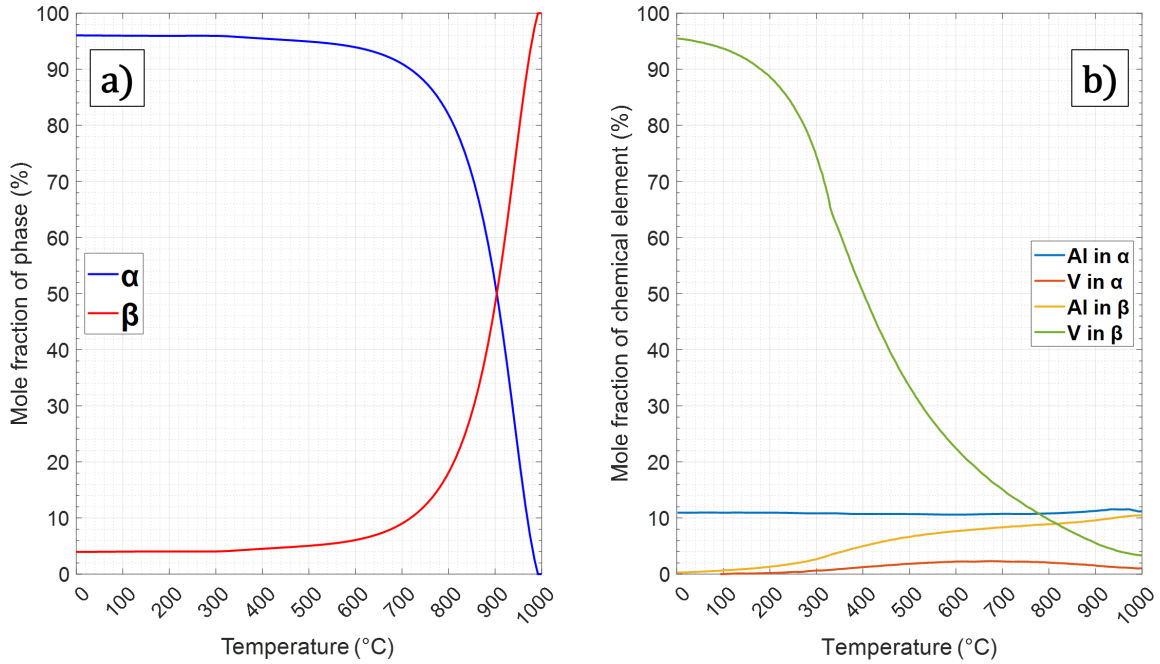

Figure 15: Thermo-Calc simulations performed using the Ti64 composition from Table 1 with the TCTI4 database to calculate: (a) the equilibrium mole fraction of α and β phases as a function of temperature, and (b) the equilibrium mole fraction of Al and V in α and β phases as a function of temperature.

The annealing temperature of post L-PBF HT plays a major role in the coarsening of α laths. As shown in Figure 8.c, the average thickness of the α laths is maintained below 1 µm for HT at 720 °C and 800 °C, but an exponential coarsening evolution is observed for HT above 860 °C. For low temperature HT (600 °C $< T <$ 800 °C), the restrained growth could be attributed to an obstructing effect of the α lath boundaries. Since the β phase fraction at equilibrium is limited ($<$ 20 %, see Figure 15.a), only a few α laths transform into β, thus limiting the growth of the remaining α laths. In contrast, for high-temperature HT (800 °C $< T < T_{beta}$), a significant fraction of α laths is transformed into β (see Figure 15.a). During the furnace cooling step, the $\beta \longrightarrow \alpha$ transformation is facilitated by the growth of the remaining α phase towards the β matrix located along the α lath boundaries, explaining the coarsening of thickness while the length of the α laths remains relatively unaffected (see scales in Figure 7). This results in a significant change in the aspect ratio of the α laths. For higher annealing temperatures, the reduction of interfacial energy may lead to the formation of globular grains during the coarsening step, as depicted in Figure 3. It should also be noted that despite the significant increase in the average α laths thickness measured for HT at higher temperatures, the distribution of the α laths thickness (see Figure 8) remains highly scattered. This highlights the fact that the resulting microstructure after HT is strongly influenced by the acicular microstructure obtained after L-PBF fabrication, with hierarchical sizes of the α' needles [20].

The influence of the utilized furnace on microstructural evolution is minimal as the thermal cycles applied are very similar between IF-HT and LF-HT (see Figure 1). Consequently, the measured β phase fraction (Figure 6.c) and average α laths thickness (Figure 8.c) show comparable results for both equipment. Only a slight reduction in α laths thickness was observed for LF-HT at high annealing temperature. The higher cooling rates achieved in LF-HT compared to IF-HT might be a contributing factor, as they allowed for a shorter time at high temperature, thereby limiting the growth of α laths [28, 68].

In conclusion, the acicular microstructure generated by L-PBF can be transformed into a close-to-equilibrium microstructure through post-processing sub-transus HT. The size of the resulting α laths, as well as the fraction of retained β phase, and hence the mechanical response of the alloy, can be optimized by selecting an appropriate annealing temperature. The closer the temperature to the transus, the higher the amount of martensite that transforms into β phase at the annealing temperature and the faster the diffusion of the alloying elements. As a result, closer temperatures to the transus lead to thicker α laths and higher β phase fractions. This trend is particularly evident under slow cooling conditions, allowing for vanadium diffusion and β phase stabilization during cooling. Based on the obtained results, the temperature range of [860 °C ; 920 °C] appears to be suitable for controlling the trade-off between α laths size and β phase fraction, thereby achieving a favorable compromise between strength and ductility.

4.2 Role of annealing temperature on alpha-case formation

Unlike the microstructural evolution, the choice of the heating furnace plays a major role in alpha-case formation. As shown in Figures 16.a and 16.b, no alpha-case was revealed by chemical etching after LF-HT, while an alpha-case layer whose depth increases with increasing temperatures was revealed after IF-HT. Figures 1.a and 1.b illustrate the significant difference in vacuum pressure attained in the industrial furnace ($< 5 \times 10^{-4}$ mbar, i.e. secondary vacuum) compared to the laboratory furnace ($< 5 \times 10^{-2}$ mbar, i.e. primary vacuum). This indicates that the furnace atmosphere, although crucial for controlling the oxidation kinetics of the Ti64 alloy at high temperatures [74, 75], is not the sole factor in preventing alpha-case formation on the components. The differences observed between IF-HT and LF-HT can be attributed to various factors, including the volumetric dimensions of the chambers and the materials used for insulation and heating elements. The industrial furnace has a much larger effective capacity (0.25 m^3) compared to the laboratory furnace (5×10^{-3} m^3), which may make maintaining air-tightness more challenging in the former. Additionally, the use of fiber/wool insulation can influence oxidation during HT (degassing), thus facilitating the formation of alpha-case.

The results presented in Figures 9 (metallography with Weck reagent), 10 (microhardness profiles), 12 (brittle layer at the edge of the rupture surface), and 13 (cracks at the surface of tensile specimens) demonstrate that the impact of the alpha-case layer is measurable through various characterization techniques. Hence, it is possible to evaluate, from each technique,

the thickness of the sub-surface layer of material affected by the presence of a higher oxygen concentration than the bulk material. The thicknesses of this so-called Oxygen Affected Zones (OAZ) measured from the aforementioned results are plotted in Figure 16.a. For the five IF-HT temperatures, the OAZ measured by different techniques are comparable, indicating that the presence of oxygen is responsible for the change in hardness and consequently the shift in the fracture mode from ductile to brittle near the surface.

The diffusion of oxygen in titanium and its alloys tends to follow parabolic kinetics [41, 76, 77]. Therefore, it can be modeled using the solution of Fick's second law in a semi-infinite solid (equation 1). This model assumes a constant concentration C_S at the surface, a constant initial concentration C_0 in the bulk of the metal, and a constant diffusion coefficient D under isothermal conditions [38, 58, 77, 78]:

$$C(x,t) = C_0 + (C_S - C_0) \times \left(1 - erf\left(\frac{x}{2\sqrt{Dt}}\right)\right) \tag{1}$$

Considering that the OAZ depth values are measured at a distance from the surface where the oxygen concentration $C(OAZ, 2h)$ is close to the bulk concentration C_0, the criterion $OAZ = 4 \times \sqrt{D \times 2h}$ was chosen. This criterion, according to equation 1, yields a ratio $(C(x,t) - C_0)/(C_S - C_0) = 1 - erf(2) \approx 0,005$. Using this criterion, the values of D for the five annealing temperatures were calculated based on the OAZ measurements obtained from different techniques, as shown in Figure 16.a. The resulting data are plotted on the Arrhenius diagram displayed in Figure 16.b and were fitted to obtain the pre-exponential factor D_0 and the activation energy Q for the diffusion of oxygen in L-PBF Ti64, using the following equation:

$$D(T) = D_0 \times \exp\left(\frac{-Q}{RT}\right) \tag{2}$$

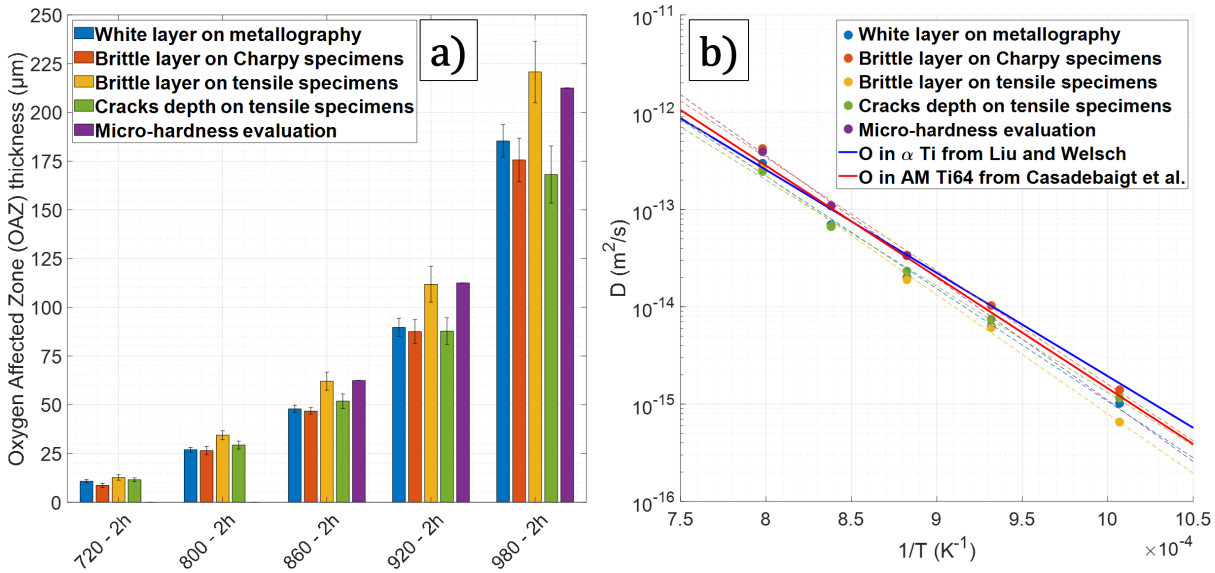

Figure 16: (a) Evaluation of the thickness of the Oxygen Affected Zone (OAZ) using various techniques, and (b) Arrhenius plot showing the oxygen diffusion coefficients in Ti64 obtained in this study compared with data from references [79] and [58].

The values D_0 and Q obtained from the fits using the OAZ data measured with different techniques are listed in Table 3. As indicated by the blue and red straight lines in Figure 16.b, the obtained values are close to those reported by Liu and Welsch for the diffusivity of oxygen in α pure titanium [79], and even closer to those found by Casadebaigt et al. for the diffusivity of oxygen in Ti64 fabricated by additive manufacturing (L-PBF and Electron Beam Melting) [58].

Measurement technique	D_0 (m^2 s^{-1})	Q (kJ mol^{-1})
White later on metallography	4.08×10^{-4}	222.7
Brittle layer on Charpy specimens	1.30×10^{-3}	233.9
Brittle layer on tensile specimens	7.08×10^{-4}	222.9
Cracks depth on tensile specimens	1.09×10^{-4}	209.0
Microhardness evaluation	4.00×10^{-3}	240.4
Mean values	$\mathbf{1.31\times10^{-3}}$	**225.8**

Table 3: Pre-exponential factors D_0 and activation energies Q calculated from the fitted data in Figure 16.b.

As direct measurements of the oxygen concentration profile were not established in this work, it is assumed that some of the indirect measurement techniques proposed may lead to an underestimation or an overestimation of the diffusivity of oxygen in L-PBF Ti64. Consequently, to simulate oxygen concentration profiles for the IF-HT conditions, the mean values of the diffusion coefficient parameters D_0 and Q were considered (see Table 3). The parameter C_0 is fixed equal to 0.48 at% (0.17 wt%), which corresponds to the bulk concentration of the Ti64 printed material used in this work and was measured by infrared absorption of combustion gases with a LECO TC-436 (O,N) analyzer. The parameter C_S is fixed at 33 at%, which is the solubility limit of oxygen in the α phase of titanium [38]. Using these parameters in equation 1, the oxygen concentration profiles in the sub-surface of IF-HT samples are simulated in Figure 17.a. The Oxygen Diffusion Zones (ODZ) indicated by black cross marks are defined as the depths where an oxygen concentration of 0.6 at% ($\approx$ 0.2 wt%) is reached. This value represents the upper limit of oxygen content in ASTM grade 5 Ti64. The vertical dashed lines indicate the depths where an oxygen concentration of 1 at% is reached. This value is referred to as the oxygen content above which the ductility of Ti64 decreases drastically [80, 81]. Interestingly, the depth values located at the positions of the dashed lines (corresponding to 1 at% oxygen concentration) are very similar to the thicknesses of the brittle layer measured on tensile specimens (see Figures 12 and 16.a). This suggests that the transition from ductile to brittle behavior is likely to occur for oxygen concentrations as low as around 1 at%, which is consistent with other literature findings [58, 80, 82]. The hardness of titanium and its alloys is sensitive to small variations in oxygen content [39, 66, 83, 84]. Therefore, the simulated oxygen concentrations displayed in Figure 17 can be compared to the microhardness values given in Figure 10. The evolution of hardness with oxygen content follows a parabolic law: Vaché and Monceau highlighted that a

linear relationship exists between hardness values and the square root of oxygen atomic percent values for commercially pure titanium and Ti-6242 α titanium alloy [41]. Figure 18 shows that such a relationship is also found for L-PBF Ti64, with consistent coefficients of determination R^2 obtained. For the three linear regressions of the microhardness values obtained from IF-HT samples annealed at 860 °C, 920 °C and 980 °C, the slopes of the fitted relations vary. This feature indicates that the microstructural evolution needs to be taken into account when evaluating oxygen hardening in Ti64 alloy. Finally, the linear regressions plotted in Figure 18 support the validity of the oxygen concentration simulation (Figure 17) and hence the reliability of the experimental coefficients found in this study for the diffusion of oxygen in L-PBF Ti64.

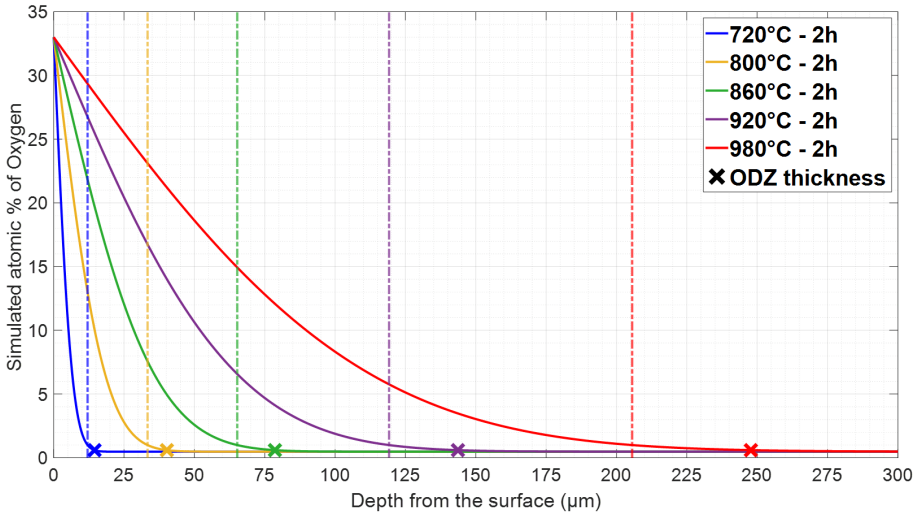

Figure 17: Simulated oxygen concentrations in the sub-surface of IF-HT samples obtained using equation 1. The vertical dash lines indicate the depths where an oxygen concentration of 1 at% is reached.

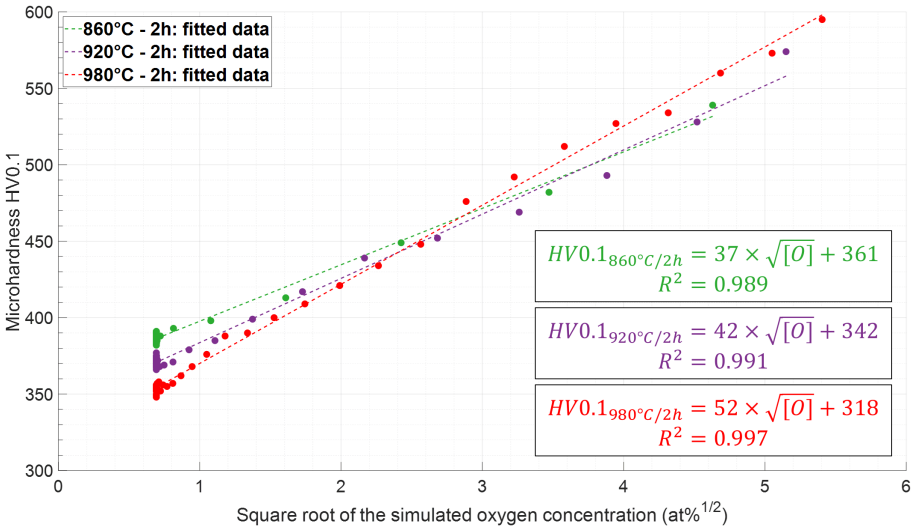

Figure 18: Microhardness values measured in the sub-surface of Ti64 samples subjected to various LF-HT shown in Figure 10, plotted as a function of the square root of the simulated oxygen atomic concentration displayed in Figure 17.

4.3 Impact of microstructural evolution on mechanical properties

Average tensile properties evaluated from stress-strain curves of vertically built IF-HT and LF-HT samples (Figure 11.a) are plotted in Figure 19. The evolution of strength (σ_y and σ_u in Figure 19.a) and hardness properties (HV_{1kg} in Figure 4) is in good agreement with the microstructural characterization performed on both IF-HT and LF-HT samples. As mentioned in section 4.1, the microstructure (prior β grains, α laths thickness, β phase fraction) obtained after IF-HT and LF-HT conditions is very similar, resulting in similar properties as well. Only a slight increase in HV_{1kg} and σ_y is noticed for LF-HT samples at higher annealing temperatures compared to IF-HT samples. This observation could be attributed to the higher cooling rates obtained for LF-HT samples, leading to a slightly finer microstructure. The hardness and σ_y of Ti64 primarily depend on the characteristic sizes of the microstructure, especially the α laths thickness [4, 28, 85]. As shown in Figure 20, a clear correlation can be established between the yield stress and/or the hardness with the inverse square root of the measured average apparent thickness of the α laths ($\bar{d}$ from Figure 8). This reveals that σ_y (hence HV) follows a Hall-Petch relationship with the α laths thickness. Similar relationships have been established in other studies for Ti64 fabricated by L-PBF [21, 68, 86], as well as with other fabrication routines [87]. From this plot and using the indicated coefficients obtained in Figure 20, it would be possible to estimate the characteristic size of the α laths from a simple hardness measurement and forecast an expected yield stress value at the same time.

The σ_u measured for LF-HT samples at higher annealing temperatures are greater than those measured for IF-HT samples. As shown in the tensile stress-strain curves in Figure 11.a, the strain hardening is limited for samples after IF-HT at 920 °C and 980 °C, as the highest measured stress values (hence σ_u) are located close to the fracture zone.

Previous studies focusing on the effects of sub-transus HT on the tensile behavior of L-PBF Ti64 parts have often reported that the closer the temperature to the transus, the higher the elongation to failure [30, 49, 52, 68]. This behavior is observed for LF-HT samples in Figure 19.b. Very high elongations to failure, comparable to those of wrought Ti64, are obtained for the highest sub-transus LF-HT temperatures. Furthermore, even though the samples in the present study were tested with their raw surface state, the elongation values are similar to those obtained with machined Ti64 L-PBF samples [88]. In contrast, the ε_f of IF-HT samples decreases for annealing temperatures of 860 °C and above. The main highlighted difference between IF-HT and LF-HT microstructures is the presence of an alpha-case at the sub-surface. Therefore, it is expected from these results that the alpha-case layer plays a major role in decreasing the ductility of the Ti64 alloy. This result emphasizes the importance of considering the heating environment when designing post L-PBF HT for Ti64 alloy. The role of alpha-case thickness on the ductility drop is further discussed in section 4.4 hereafter.

The impact properties measured on Charpy V-notch specimens (Figure 11.b and table 19) show a similar trend in elongation to failure for IF-HT and LF-HT below 860 °C. However, contrary to ductility, the resilience of the material after IF-HT is slightly improved at annealing temperatures of 860 °C and above. Nevertheless, the values obtained for samples after LF-HT at 860 °C and above are significantly better than the ones obtained after IF-HT. The improved resilience of

LF-HT samples aligns with the coarsening of α laths and the increased β phase fraction, as the impact toughness of Ti64 alloy is primarily influenced by the size of microstructural elements that cause bifurcation of the crack propagation path [89, 90]. However, the highest impact toughness obtained in this work (24.8±1.2 J) is still lower than the $\approx 30-40$ J impact toughness measured for Ti64 fabricated using conventional processes that exhibit a typical lamellar, equiaxed, or bimodal microstructure [63, 89–91].

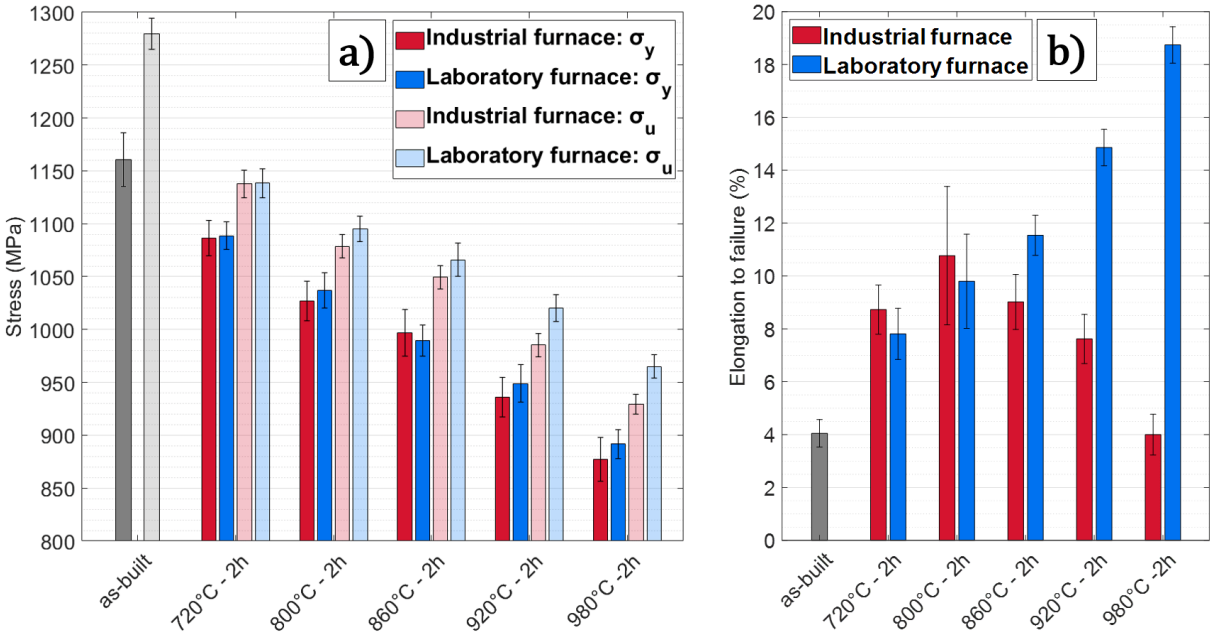

Figure 19: Evolution of tensile properties of the vertically built samples in the as-built condition and subjected to various IF-HT and LF-HT: (a) Yield stress σ_y and ultimate tensile strenght σ_u, (b) Elongation to failure ε_f.

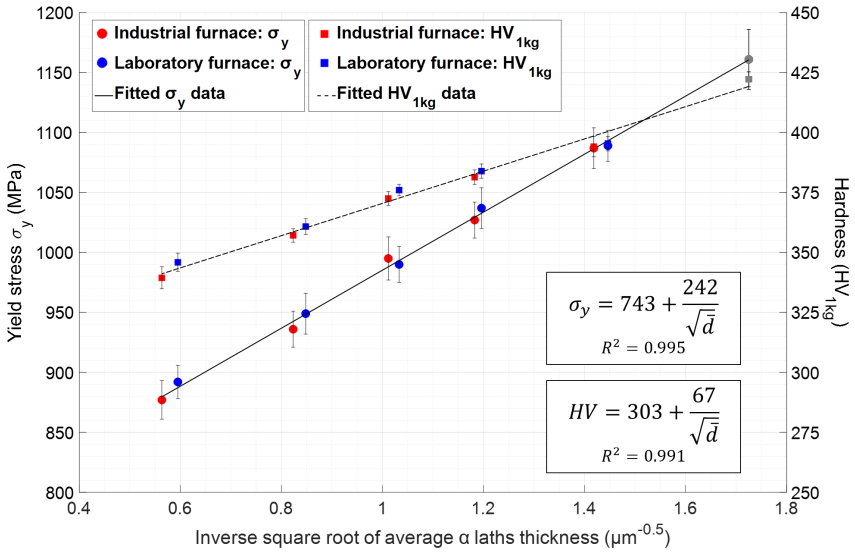

Figure 20: Evolution of the measured yield stress and hardness as a function of the inverse square root of the measured average apparent thickness of the α laths.

4.4 Impact of alpha-case depth on embrittlement

Figures 13 indicate that cracks are generated along the gauge length surface of the sample during the tensile test and propagate in a brittle manner (see Figure 12) across the alpha-case thickness, which corresponds to the area with the highest oxygen concentration in the material (see Figure 17). As shown in Figure 19.b, the presence of an alpha-case thickness of approximately $10 - 25$ µm (IF-HT at 720 °C and 800 °C) does not seem to significantly influence the elongation to failure for 3 mm thick tensile samples. However, for alpha-case thicknesses of approximately 50 µm (IF-HT at 860 °C), ε_f is slightly lower compared to the LF-HT sample without alpha-case. Finally, alpha-case thicknesses of approximately $\approx 100 - 200$ µm (IF-HT at 920 °C and 980 °C), which cause the presence of deeper strain-induced cracks, are extremely detrimental to the ductility of the sample: ε_f is respectively half and four times lower than for similar samples without alpha-case.

From the results presented in this work, it is, however, difficult to understand the mechanisms explaining the impact of the deeper strain-induced cracks on ductility. A first hypothesis is that the stress concentration at the crack tips is high enough to initiate crack propagation in the bulk material and lead to premature failure starting from the surface. However, as most of the cracks presented in Figure 13 are blunt and do not propagate beyond the alpha-case, this assumption is questionable. A second hypothesis is that the damage is initiated in the bulk, but because of the stress concentration at the crack tips, the material's ability to plastically deform is drastically reduced, leading to sample fracture with little plastic strain necessary. To verify the validity of either hypothesis, *in situ* tensile tests combined with X-ray tomography could be performed to determine whether the damage initiates at the crack tips or in the bulk [92].

The impact energy values obtained suggest that for IF-HT at the highest annealing temperatures, the brittle layer limits the length of the crack propagation path and, therefore, the material's ability to absorb energy. However, the impact toughness of the material is less affected by oxygen embrittlement compared to the achievable ductility under tensile loading: the IF-HT condition with the worst f exhibits the best KV in this study. This result could be explained by a "size-effect" of the sample: the ≈ 200 µm alpha-case for IF-HT at 980 °C affects only 5 % of the 8 mm thick normalized Charpy V-notch impact samples, while it affects more than 13 % of the 3 mm thick dog-bone shape tensile specimens. Furthermore, it is generally reported that fracture toughness is a combination of ductility and strength of the material. This illustrates that alpha-case embrittlement does not show the same effects on the material properties depending on the loading mode.

One of the key findings of this study is the evidence of visible cracks under SEM in the alpha-case layer of a tensile sample loaded in the elastic domain (Figure 14). These cracks started to be detectable at tensile stress values that are half the measured yield stress of the material. This result suggests that, besides the ductility decrease for the highest annealing temperatures, alpha-case embrittlement could be highly detrimental to the fatigue performance of Ti64 alloy fabricated by L-PBF and subjected to an industrial post-processing HT with a partially contained oxidizing environment.

5 Conclusions

In this study, post Laser Powder Bed Fusion process (L-PBF) heat-treatments (HT) on Ti-6Al-4V (Ti64) samples with various sub-transus annealing temperatures were performed. To significantly modify the atmo- sphere, the HT were conducted using an industrial furnace (IF-HT conditions) and a laboratory furnace (LF-HT conditions). The objective of this study was to investigate the effects of microstructural evolution and alpha-case formation on the mechanical properties of L-PBF Ti64 parts that will not undergo any machining after fabrication. The following conclusions were drawn from this work:

- The as-built microstructure consists of entangled α' martensitic needles that form within prior β grains during the rapid cooling of the L-PBF process. Sub-transus HT for 2 hours between 720 °C and 980 °C, followed by slow furnace cooling, results in the decomposition of martensite into $\alpha + \beta$ equilibrium phases while preserving the prior β grain structure. Quantitative measurements revealed that the higher the annealing temperature, the greater the β phase fraction and the growth of α grains. The bulk microstructures obtained for IF-HT and LF-HT were nearly identical.

- The IF-HT samples displayed a notable increase in alpha-case thickness with higher annealing temperatures, resulting in significantly elevated surface hardness. On the contrary, no alpha-case formation was observed in the LF-HT samples. Oxygen concentration exceeding 1 at% led to a transition from ductile to brittle fracture mode, causing the appearance of a brittle layer on the edge of the fracture surface in the mechanical specimens. Tensile samples exhibited crack formation along the gauge length surface, which propagated through the alpha-case.

- In the as-built condition, the tensile properties exhibit very high strength but poor ductility. The microstructural evolution during sub-transus HT helps achieve a balance between strength and ductility, with the yield stress being governed by the thickness of the α laths through the Hall-Petch mechanism. However, the ductility of IF-HT samples decreases significantly for alpha-case depths $\geq$ 50 µm. For IF-HT at 800 °C for 2 h, a favorable compromise is achieved, resulting in a strong material ($\sigma_y > 1\,000$ MPa) with good ductility ($\varepsilon > 10$ %) when the tensile load is parallel to the building direction, with minimal effects of the approximately 25 µm alpha-case on the tensile properties. On the other hand, without any alpha-case, the ductility can be further increased with higher temperatures, as demonstrated in LF-HT samples. The alloy exhibits a similar evolution in terms of ductility and impact toughness.

- Cracks formed at the sample surface during the tensile test are "strain-induced", and their opening rate at the surface is primarily controlled by the level of plastic strain. However, *in situ* investigations have revealed that these cracks actually initiate in the elastic domain, even at stress levels lower than half the yield stress. Therefore, further research should be undertaken to explore the potential influence of the alpha-case on the fatigue behavior of Ti64 alloy fabricated using L-PBF.

Data availability

The raw/processed data required to reproduce these findings cannot be shared at this time as the data also forms part of an ongoing study.

CRediT authorship contribution statement

Quentin Gaillard: Conceptualisation, Writing - Original Draft, Investigation, Visualisation. **Xavier Boulnat**: Conceptualisation, Supervision, Writing - Review & Editing. **Sophie Cazottes**: Investigation, Supervision, Writing - Review & Editing. **Sylvain Dancette**: Supervision, Writing - Review & Editing. **Christophe Desrayaud**: Supervision, Validation, Funding acquisition.

Declaration of Competing Interest

The authors declare that they have no known competing financial interests or personal relationships that could have appeared to influence the work reported in this paper.

Acknowledgments

This work, conducted at LGF and MATEIS laboratories, falls within the framework of the AEROPRINT project, which received support from the Auvergne-Rhône-Alpes Region and the the company Dassault Aviation, France. The authors are grateful for their financial support and extend special thanks to the project team at the Argonay production site for fabricating the samples used in this study. Additionally, the authors would like to acknowledge the valuable contributions of Pauline Chanin-Lambert and Maryline Mondon for their assistance with the laboratory furnace setup, Nathalie Peillon for conducting XRD measurements, Séverine Girard-Insardi for supervising tensile and impact tests, Gilles Blanc for overseeing metallographic preparation, and Florian Steinhilber and Amélie Larguier for their involvement during in situ tensile tests. The authors also express their appreciation to David Piot and Guillaume Kermouche for engaging in numerous fruitful discussions.

References

[1] M. J. Donachie. *Titanium: A Technical Guide*. 2nd ed. Materials Park, OH: ASM International, 2000. ISBN: 978-0-87170-686-7.

[2] R. Boyer. "An Overview on the Use of Titanium in the Aerospace Industry". In: *Materials Science and Engineering: A* 213.1-2 (1996), pp. 103–114. ISSN: 09215093. DOI: 10.1016/0921-5093(96)10233-1.

[3] M. Peters, J. Kumpfert, C. Ward, and C. Leyens. "Titanium Alloys for Aerospace Applications". In: *Advanced Engineering Materials* 5.6 (2003), pp. 419–427. ISSN: 14381656, 15272648. DOI: 10.1002/adem.200310095.

[4] G. Lütjering. "Influence of Processing on Microstructure and Mechanical Properties of (A+β) Titanium Alloys". In: *Materials Science and Engineering: A* 243.1-2 (1998), pp. 32–45. ISSN: 09215093. DOI: 10.1016/S0921-5093(97)00778-8.

[5] I. Weiss, F. H. Froes, D. Eylon, and G. E. Welsch. "Modification of Alpha Morphology in Ti-6Al-4V by Thermomechanical Processing". In: *Metallurgical Transactions A* 17.11 (1986), pp. 1935–1947. ISSN: 0360-2133, 1543-1940. DOI: 10.1007/BF02644991.

[6] T. DebRoy, H. Wei, J. Zuback, T. Mukherjee, J. Elmer, J. Milewski, A. Beese, A. Wilson-Heid, A. De, and W. Zhang. "Additive Manufacturing of Metallic Components – Process, Structure and Properties". In: *Progress in Materials Science* 92 (2018), pp. 112–224. ISSN: 00796425. DOI: 10.1016/j.pmatsci.2017.10.001.

[7] S. Liu and Y. C. Shin. "Additive Manufacturing of Ti6Al4V Alloy: A Review". In: *Materials & Design* 164 (2019), p. 107552. ISSN: 02641275. DOI: 10.1016/j.matdes.2018.107552.

[8] B. Song, S. Dong, B. Zhang, H. Liao, and C. Coddet. "Effects of Processing Parameters on Microstructure and Mechanical Property of Selective Laser Melted Ti6Al4V". In: *Materials & Design* 35 (2012), pp. 120–125. ISSN: 02613069. DOI: 10.1016/j.matdes.2011.09.051.

[9] A. K. Singla, M. Banerjee, A. Sharma, J. Singh, A. Bansal, M. K. Gupta, N. Khanna, A. Shahi, and D. K. Goyal. "Selective Laser Melting of Ti6Al4V Alloy: Process Parameters, Defects and Post-Treatments". In: *Journal of Manufacturing Processes* 64 (2021), pp. 161–187. ISSN: 15266125. DOI: 10.1016/j.jmapro.2021.01.009.

[10] P. Edwards and M. Ramulu. "Fatigue Performance Evaluation of Selective Laser Melted Ti–6Al–4V". In: *Materials Science and Engineering: A* 598 (2014), pp. 327–337. ISSN: 09215093. DOI: 10.1016/j.msea.2014.01.041.

[11] C. Qiu, N. J. Adkins, and M. M. Attallah. "Microstructure and Tensile Properties of Selectively Laser-Melted and of HIPed Laser-Melted Ti–6Al–4V". In: *Materials Science and Engineering: A* 578 (2013), pp. 230–239. ISSN: 09215093. DOI: 10.1016/j.msea.2013.04.099.

[12] I. Yadroitsev, P. Krakhmalev, I. Yadroitsava, and A. Du Plessis. "Qualification of Ti6Al4V ELI Alloy Produced by Laser Powder Bed Fusion for Biomedical Applications". In: *JOM* 70.3 (2018), pp. 372–377. ISSN: 1047-4838, 1543-1851. DOI: 10.1007/s11837-017-2655-5.

[13] Q. Gaillard, S. Cazottes, X. Boulnat, S. Dancette, and C. Desrayaud. "Microstructure, Texture and Mechanical Properties with Raw Surface States of Ti-6Al-4V Parts Built by L-PBF". In: *Procedia CIRP* 108 (2022), pp. 698–703. ISSN: 22128271. DOI: 10.1016/j.procir.2022.03.108.

[14] P. Mercelis and J.-P. Kruth. "Residual Stresses in Selective Laser Sintering and Selective Laser Melting". In: *Rapid Prototyping Journal* 12.5 (2006), pp. 254–265. ISSN: 1355-2546. DOI: 10.1108/13552540610707013.

[15] L. Anderson, A. Venter, B. Vrancken, D. Marais, J. Van Humbeeck, and T. Becker. "Investigating the Residual Stress Distribution in Selective Laser Melting Produced Ti-6Al-4V Using Neutron Diffraction". In: *Meca Sens 2017*. Vol. 4. Materials Research Proceedings, 2018, pp. 73–78. DOI: 10.21741/9781945291678-11.

[16] B. Ahmad, S. O. van der Veen, M. E. Fitzpatrick, and H. Guo. "Residual Stress Evaluation in Selective-Laser-Melting Additively Manufactured Titanium (Ti-6Al-4V) and Inconel 718 Using the Contour Method and Numerical Simulation". In: *Additive Manufacturing* 22 (2018), pp. 571–582. ISSN: 22148604. DOI: 10.1016/j.addma.2018.06.002.

[17] B. Vrancken, V. Cain, R. Knutsen, and J. Van Humbeeck. "Residual Stress via the Contour Method in Compact Tension Specimens Produced via Selective Laser Melting". In: *Scripta Materialia* 87 (2014), pp. 29–32. ISSN: 13596462. DOI: 10.1016/j.scriptamat.2014.05.016.

[18] V. Cain, L. Thijs, J. Van Humbeeck, B. Van Hooreweder, and R. Knutsen. "Crack Propagation and Fracture Toughness of Ti6Al4V Alloy Produced by Selective Laser Melting". In: *Additive Manufacturing* 5 (2015), pp. 68–76. ISSN: 22148604. DOI: 10.1016/j.addma.2014.12.006.

[19] A. K. Syed, B. Ahmad, H. Guo, T. Machry, D. Eatock, J. Meyer, M. E. Fitzpatrick, and X. Zhang. "An Experimental Study of Residual Stress and Direction-Dependence of Fatigue Crack Growth Behaviour in as-Built and Stress-Relieved Selective-Laser-Melted Ti6Al4V". In: *Materials Science and Engineering: A* 755 (2019), pp. 246–257. ISSN: 09215093. DOI: 10.1016/j.msea.2019.04.023.

[20] J. Yang, H. Yu, J. Yin, M. Gao, Z. Wang, and X. Zeng. "Formation and Control of Martensite in Ti-6Al-4V Alloy Produced by Selective Laser Melting". In: *Materials & Design* 108 (2016), pp. 308–318. ISSN: 02641275. DOI: 10.1016/j.matdes.2016.06.117.

[21] S. Cao, R. Chu, X. Zhou, K. Yang, Q. Jia, C. V. S. Lim, A. Huang, and X. Wu. "Role of Martensite Decomposition in Tensile Properties of Selective Laser Melted Ti-6Al-4V". In: *Journal of Alloys and Compounds* 744 (2018), pp. 357–363. ISSN: 09258388. DOI: 10.1016/j.jallcom.2018.02.111.

[22] W. Xu, M. Brandt, S. Sun, J. Elambasseril, Q. Liu, K. Latham, K. Xia, and M. Qian. "Additive Manufacturing of Strong and Ductile Ti–6Al–4V by Selective Laser Melting via in Situ Martensite Decomposition". In: *Acta Materialia* 85 (2015), pp. 74–84. ISSN: 13596454. DOI: 10.1016/j.actamat.2014.11.028.

[23] T. Vilaro, C. Colin, and J. D. Bartout. "As-Fabricated and Heat-Treated Microstructures of the Ti-6Al-4V Alloy Processed by Selective Laser Melting". In: *Metallurgical and Materials Transactions A* 42.10 (2011), pp. 3190–3199. ISSN: 1073-5623, 1543-1940. DOI: 10.1007/s11661-011-0731-y.

[24] M. Simonelli, Y. Y. Tse, and C. Tuck. "On the Texture Formation of Selective Laser Melted Ti-6Al-4V". In: *Metallurgical and Materials Transactions A* 45.6 (2014), pp. 2863–2872. ISSN: 1073-5623, 1543-1940. DOI: 10.1007/s11661-014-2218-0.

[25] C. V. Funch, A. Palmas, K. Somlo, E. H. Valente, X. Cheng, K. Poulios, M. Villa, M. A. Somers, and T. L. Christiansen. "Targeted Heat Treatment of Additively Manufactured Ti-6Al-4V for Controlled Formation of Bi-lamellar Microstructures". In: *Journal of Materials Science & Technology* 81 (2021), pp. 67–76. ISSN: 10050302. DOI: 10.1016/j.jmst.2021.01.004.

[26] G. Kasperovich and J. Hausmann. "Improvement of Fatigue Resistance and Ductility of TiAl6V4 Processed by Selective Laser Melting". In: *Journal of Materials Processing Technology* 220 (2015), pp. 202–214. ISSN: 09240136. DOI: 10.1016/j.jmatprotec.2015.01.025.

[27] S. Leuders, M. Thöne, A. Riemer, T. Niendorf, T. Tröster, H. Richard, and H. Maier. "On the Mechanical Behaviour of Titanium Alloy TiAl6V4 Manufactured by Selective Laser Melting: Fatigue Resistance and Crack Growth Performance". In: *International Journal of Fatigue* 48 (2013), pp. 300–307. ISSN: 01421123. DOI: 10.1016/j.ijfatigue.2012.11.011.

[28] B. Vrancken, L. Thijs, J.-P. Kruth, and J. Van Humbeeck. "Heat Treatment of Ti6Al4V Produced by Selective Laser Melting: Microstructure and Mechanical Properties". In: *Journal of Alloys and Compounds* 541 (2012), pp. 177–185. ISSN: 09258388. DOI: 10.1016/j.jallcom.2012.07.022.

[29] G. Ter Haar and T. Becker. "Selective Laser Melting Produced Ti-6Al-4V: Post-Process Heat Treatments to Achieve Superior Tensile Properties". In: *Materials* 11.1 (2018), p. 146. ISSN: 1996-1944. DOI: 10.3390/ma11010146.

[30] D. Wang, H. Wang, X. Chen, Y. Liu, D. Lu, X. Liu, and C. Han. "Densification, Tailored Microstructure, and Mechanical Properties of Selective Laser Melted Ti–6Al–4V Alloy via Annealing Heat Treatment". In: *Micromachines* 13.2 (2022), p. 331. ISSN: 2072-666X. DOI: 10.3390/mi13020331.

[31] Z. Qu, Z. Zhang, Y. Zhu, R. Liu, S. Lu, S. Li, Q. Duan, B. Zhang, M. Zhao, J. Eckert, and Z. Zhang. "Coupling Effects of Microstructure and Defects on the Fatigue Properties of Laser Powder Bed Fusion Ti-6Al-4V". In: *Additive Manufacturing* 61 (2023), p. 103355. ISSN: 22148604. DOI: 10.1016/j.addma.2022.103355.

[32] P. Kumar and U. Ramamurty. "Microstructural Optimization through Heat Treatment for Enhancing the Fracture Toughness and Fatigue Crack Growth Resistance of Selective Laser Melted Ti 6Al 4V Alloy". In: *Acta Materialia* 169 (2019), pp. 45–59. ISSN: 13596454. DOI: 10.1016/j.actamat.2019.03.003.

[33] ASTM International. *Specification for Additive Manufacturing Titanium-6 Aluminum-4 Vanadium with Powder Bed Fusion*. Tech. rep. ASTM F2924-14. ASTM International, 2021. DOI: 10.1520/F2924-14R21.

[34] Y. Liu, Y. Yang, and D. Wang. "A Study on the Residual Stress during Selective Laser Melting (SLM) of Metallic Powder". In: *The International Journal of Advanced Manufacturing Technology* 87.1-4 (2016), pp. 647–656. ISSN: 0268-3768, 1433-3015. DOI: 10.1007/s00170-016-8466-y.

[35] J. Unnam, R. N. Shenoy, and R. K. Clark. "Oxidation of Commercial Purity Titanium". In: *Oxidation of Metals* 26.3-4 (1986), pp. 231–252. ISSN: 0030-770X, 1573-4889. DOI: 10.1007/BF00659186.

[36] H. Guleryuz and H. Cimenoglu. "Oxidation of Ti–6Al–4V Alloy". In: *Journal of Alloys and Compounds* 472.1-2 (2009), pp. 241–246. ISSN: 09258388. DOI: 10.1016/j.jallcom.2008.04.024.

[37] A. Casadebaigt, J. Hugues, and D. Monceau. "Influence of Microstructure and Surface Roughness on Oxidation Kinetics at 500–600 °C of Ti–6Al–4V Alloy Fabricated by Additive Manufacturing". In: *Oxidation of Metals* 90.5-6 (2018), pp. 633–648. ISSN: 0030-770X, 1573-4889. DOI: 10.1007/s11085-018-9859-0.

[38] C. Shamblen and T. Redden. "Air Contamination and Embrittlement of Titanium Alloys". In: *The Science, Technology and Application of Titanium*. Elsevier, 1970, pp. 199–208. ISBN: 978-0-08-006564-9. DOI: 10.1016/B978-0-08-006564-9.50027-0.

[39] M. L. Wasz, F. R. Brotzen, R. B. McLellan, and A. J. Griffin. "Effect of Oxygen and Hydrogen on Mechanical Properties of Commercial Purity Titanium". In: *International Materials Reviews* 41.1 (1996), pp. 1–12. ISSN: 0950-6608, 1743-2804. DOI: 10.1179/imr.1996.41.1.1.

[40] R. Gaddam, B. Sefer, R. Pederson, and M.-L. Antti. "Study of Alpha-Case Depth in Ti-6Al-2Sn-4Zr-2Mo and Ti-6Al-4V". In: *IOP Conference Series: Materials Science and Engineering* 48 (2013), p. 012002. ISSN: 1757-8981, 1757-899X. DOI: 10.1088/1757-899X/48/1/012002.

[41] N. Vaché and D. Monceau. "Oxygen Diffusion Modeling in Titanium Alloys: New Elements on the Analysis of Microhardness Profiles". In: *Oxidation of Metals* 93.1-2 (2020), pp. 215–227. ISSN: 0030-770X, 1573-4889. DOI: 10.1007/s11085-020-09956-9.

[42] E. Dong, W. Yu, and Q. Cai. "Alpha-Case Kinetics and High Temperature Plasticity of Ti-6Al-4V Alloy Oxidized in Different Phase Regions". In: *Procedia Engineering* 207 (2017), pp. 2149–2154. ISSN: 18777058. DOI: 10.1016/j.proeng.2017.10.973.

[43] P. Seth, J. S. Jha, A. Alankar, and S. K. Mishra. "Alpha-Case Formation in Ti–6Al–4V in a Different Oxidizing Environment and Its Effect on Tensile and Fatigue Crack Growth Behavior". In: *Oxidation of Metals* 97.1-2 (2022), pp. 77–95. ISSN: 0030-770X, 1573-4889. DOI: 10.1007/s11085-021-10079-y.

[44] L.-A. Chicos, S. M. Zaharia, C. Lancea, M. A. Pop, I. Cañadas, J. Rodríguez, and J. Galindo. "Concentrated Solar Energy Used for Heat Treatment of Ti6Al4V Alloy Manufactured by Selective Laser Melting". In: *Solar Energy* 173 (2018), pp. 76–88. ISSN: 0038092X. DOI: 10.1016/j.solener.2018.07.069.

[45] A. Díaz, J. Alegre, I. Cuesta, E. Martínez-Pañeda, and Z. Zhang. "Notch Fracture Predictions Using the Phase Field Method for Ti-6Al-4V Produced by Selective Laser Melting after Different Post-Processing Conditions". In: *Theoretical and Applied Fracture Mechanics* 121 (2022), p. 103510. ISSN: 01678442. DOI: 10.1016/j.tafmec.2022.103510.

[46] T. Voisin, N. P. Calta, S. A. Khairallah, J.-B. Forien, L. Balogh, R. W. Cunningham, A. D. Rollett, and Y. M. Wang. "Defects-Dictated Tensile Properties of Selective Laser Melted Ti-6Al-4V". In: *Materials & Design* 158 (2018), pp. 113–126. ISSN: 02641275. DOI: 10.1016/j.matdes.2018.08.004.

[47] F. Niessen, T. Nyyssönen, A. A. Gazder, and R. Hielscher. "Parent Grain Reconstruction from Partially or Fully Transformed Microstructures in *MTEX*". In: *Journal of Applied Crystallography* 55.1 (2022), pp. 180–194. ISSN: 1600-5767. DOI: 10.1107/S1600576721011560.

[48] M. Simonelli, Y. Y. Tse, and C. Tuck. "Microstructure of Ti-6Al-4V Produced by Selective Laser Melting". In: *Journal of Physics: Conference Series* 371 (2012), p. 012084. ISSN: 1742-6596. DOI: 10.1088/1742-6596/371/1/012084.

[49] X. Yan, S. Yin, C. Chen, C. Huang, R. Bolot, R. Lupoi, M. Kuang, W. Ma, C. Coddet, H. Liao, and M. Liu. "Effect of Heat Treatment on the Phase Transformation and Mechanical Properties of Ti6Al4V Fabricated by Selective Laser Melting". In: *Journal of Alloys and Compounds* 764 (2018), pp. 1056–1071. ISSN: 09258388. DOI: 10.1016/j.jallcom.2018.06.076.

[50] A. Borbély, A. Aoufi, and D. Becht. "X-Ray Methods for Strain Energy Evaluation of Dislocated Crystals". In: *Journal of Applied Crystallography* 56.1 (2023), pp. 254–262. ISSN: 1600-5767. DOI: 10.1107/S1600576722012262.

[51] M. Fitzpatrick, A. Fry, P. Holdway, F. Kandil, J. Shackleton, and L. Suominen. *Determination of Residual Stresses by X-ray Diffraction*. Report/Guide 52. 2005.

[52] P. Tao, H.-x. Li, B.-y. Huang, Q.-d. Hu, S.-l. Gong, and Q.-y. Xu. "Tensile Behavior of Ti-6Al-4V Alloy Fabricated by Selective Laser Melting: Effects of Microstructures and as-Built Surface Quality". In: *China Foundry* 15.4 (2018), pp. 243–252. ISSN: 1672-6421, 2365-9459. DOI: 10.1007/s41230-018-8064-8.

[53] C. de Formanoir, S. Michotte, O. Rigo, L. Germain, and S. Godet. "Electron Beam Melted Ti–6Al–4V: Microstructure, Texture and Mechanical Behavior of the as-Built and Heat-Treated Material". In: *Materials Science and Engineering: A* 652 (2016), pp. 105–119. ISSN: 09215093. DOI: 10.1016/j.msea.2015.11.052.

[54] L. Facchini, E. Magalini, P. Robotti, A. Molinari, S. Höges, and K. Wissenbach. "Ductility of a Ti-6Al-4V Alloy Produced by Selective Laser Melting of Prealloyed Powders". In: *Rapid Prototyping Journal* 16.6 (2010), pp. 450–459. ISSN: 1355-2546. DOI: 10.1108/13552541011083371.

[55] W. Burgers. "On the Process of Transition of the Cubic-Body-Centered Modification into the Hexagonal-Close-Packed Modification of Zirconium". In: *Physica* 1.7-12 (1934), pp. 561–586. ISSN: 00318914. DOI: 10.1016/S0031-8914(34)80244-3.

[56] J. Yang, H. Yu, Z. Wang, and X. Zeng. "Effect of Crystallographic Orientation on Mechanical Anisotropy of Selective Laser Melted Ti-6Al-4V Alloy". In: *Materials Characterization* 127 (2017), pp. 137–145. ISSN: 10445803. DOI: 10.1016/j.matchar.2017.01.014.

[57] Z. Wang, A. D. Stoica, D. Ma, and A. M. Beese. "Stress Relaxation Behavior and Mechanisms in Ti-6Al-4V Determined via in Situ Neutron Diffraction: Application to Additive Manufacturing". In: *Materials Science and Engineering: A* 707 (2017), pp. 585–592. ISSN: 09215093. DOI: 10.1016/j.msea.2017.09.071.

[58] A. Casadebaigt, J. Hugues, and D. Monceau. "High Temperature Oxidation and Embrittlement at 500–600 °C of Ti-6Al-4V Alloy Fabricated by Laser and Electron Beam Melting". In: *Corrosion Science* 175 (2020), p. 108875. ISSN: 0010938X. DOI: 10.1016/j.corsci.2020.108875.

[59] P. Kumar, O. Prakash, and U. Ramamurty. "Micro-and Meso-Structures and Their Influence on Mechanical Properties of Selectively Laser Melted Ti-6Al-4V". In: *Acta Materialia* 154 (2018), pp. 246–260. ISSN: 13596454. DOI: 10.1016/j.actamat.2018.05.044.

[60] M. Simonelli, Y. Tse, and C. Tuck. "Effect of the Build Orientation on the Mechanical Properties and Fracture Modes of SLM Ti–6Al–4V". In: *Materials Science and Engineering: A* 616 (2014), pp. 1–11. ISSN: 09215093. DOI: 10.1016/j.msea.2014.07.086.

[61] E. Yasa, J. Deckers, J.-P. Kruth, M. Rombouts, and J. Luyten. "Charpy Impact Testing of Metallic Selective Laser Melting Parts". In: *Virtual and Physical Prototyping* 5.2 (2010), pp. 89–98. ISSN: 1745-2759, 1745-2767. DOI: 10.1080/17452751003703894.

[62] A. M. Muiruri, M. Maringa, W. du Preez, and L. Masu. "Variation of Impact Toughness of As-Built DMLS TI6AL4V (ELI) Specimens with Temperature". In: *South African Journal of Industrial Engineering* 29.3 (2018). ISSN: 22247890. DOI: 10.7166/29-3-2076.

[63] M.-W. Wu and P.-H. Lai. "The Positive Effect of Hot Isostatic Pressing on Improving the Anisotropies of Bending and Impact Properties in Selective Laser Melted Ti-6Al-4V Alloy". In: *Materials Science and Engineering: A* 658 (2016), pp. 429–438. ISSN: 09215093. DOI: 10.1016/j.msea.2016.02.023.

[64] M.-W. Wu, P.-H. Lai, and J.-K. Chen. "Anisotropy in the Impact Toughness of Selective Laser Melted Ti–6Al–4V Alloy". In: *Materials Science and Engineering: A* 650 (2016), pp. 295–299. ISSN: 09215093. DOI: 10.1016/j.msea.2015.10.045.

[65] L. Bendersky and A. Rosen. "The Effect of Exposure on Fracture of Ti-6AL-4V Alloy". In: *Engineering Fracture Mechanics* 13.1 (1980), pp. 111–118. ISSN: 00137944. DOI: 10.1016/0013-7944(80)90046-6.

[66] H. Ogden and R. Jaffee. *The Effects of Carbon, Oxygen, and Nitrogen on the Mechanical Properties of Titanium and Titanium Alloys*. Tech. rep. TML-20, 4370612. 1955, TML–20, 4370612. DOI: 10.2172/4370612.

[67] L. Thijs, F. Verhaeghe, T. Craeghs, J. V. Humbeeck, and J.-P. Kruth. "A Study of the Microstructural Evolution during Selective Laser Melting of Ti–6Al–4V". In: *Acta Materialia* 58.9 (2010), pp. 3303–3312. ISSN: 13596454. DOI: 10.1016/j.actamat.2010.02.004.

[68] X.-Y. Zhang, G. Fang, S. Leeflang, A. J. Böttger, A. A. Zadpoor, and J. Zhou. "Effect of Subtransus Heat Treatment on the Microstructure and Mechanical Properties of Additively Manufactured Ti-6Al-4V Alloy". In: *Journal of Alloys and Compounds* 735 (2018), pp. 1562–1575. ISSN: 09258388. DOI: 10.1016/j.jallcom.2017.11.263.

[69] J. Elmer, T. Palmer, S. Babu, and E. Specht. "In Situ Observations of Lattice Expansion and Transformation Rates of α and β Phases in Ti–6Al–4V". In: *Materials Science and Engineering: A* 391.1-2 (2005), pp. 104–113. ISSN: 09215093. DOI: 10.1016/j.msea.2004.08.084.

[70] P. Pietrokowsky and P. Duwez. "Partial Titanium-Vanadium Phase Diagram". In: *JOM* 4.6 (1952), pp. 627–630. ISSN: 1047-4838, 1543-1851. DOI: 10.1007/BF03397732.

[71] S. Mironov, M. Murzinova, S. Zherebtsov, G. Salishchev, and S. Semiatin. "Microstructure Evolution during Warm Working of Ti–6Al–4V with a Colony-α Microstructure". In: *Acta Materialia* 57.8 (2009), pp. 2470–2481. ISSN: 13596454. DOI: 10.1016/j.actamat.2009.02.016.

[72] S. Suri, G. Viswanathan, T. Neeraj, D.-H. Hou, and M. Mills. "Room Temperature Deformation and Mechanisms of Slip Transmission in Oriented Single-Colony Crystals of an α/β Titanium Alloy". In: *Acta Materialia* 47.3 (1999), pp. 1019–1034. ISSN: 13596454. DOI: 10.1016/S1359-6454(98)00364-4.

[73] Y. Zheng, R. E. Williams, G. B. Viswanathan, W. A. Clark, and H. L. Fraser. "Determination of the Structure of α-β Interfaces in Metastable β-Ti Alloys". In: *Acta Materialia* 150 (2018), pp. 25–39. ISSN: 13596454. DOI: 10.1016/j.actamat.2018.03.003.

[74] Y. Combres. "Traitements thermiques des alliages de titane". In: *Techniques de l'ingénieur*. Matériaux — Traitement des métaux M1335 V3 (2013).

[75] B. Öztürk, L. Mengis, D. Dickes, U. Glatzel, and M. C. Galetz. "Influence of Water Vapor and Temperature on the Oxide Scale Growth and Alpha-Case Formation in Ti-6Al-4V Alloy". In: *Oxidation of Metals* 97.3-4 (2022), pp. 241–260. ISSN: 0030-770X, 1573-4889. DOI: 10.1007/s11085-021-10088-x.

[76] Z. Liu and G. Welsch. "Effects of Oxygen and Heat Treatment on the Mechanical Properties of Alpha and Beta Titanium Alloys". In: *Metallurgical Transactions A* 19.3 (1988), pp. 527–542. ISSN: 0360-2133, 1543-1940. DOI: 10.1007/BF02649267.

[77] N. Vaché, Y. Cadoret, B. Dod, and D. Monceau. "Modeling the Oxidation Kinetics of Titanium Alloys: Review, Method and Application to Ti-64 and Ti-6242s Alloys". In: *Corrosion Science* 178 (2021), p. 109041. ISSN: 0010938X. DOI: 10.1016/j.corsci.2020.109041.

[78] C. Ciszak, D. Monceau, and C. Desgranges. "Modelling the High Temperature Oxidation of Titanium Alloys: Development of a New Numerical Tool PyTiOx". In: *Corrosion Science* 176 (2020), p. 109005. ISSN: 0010938X. DOI: 10.1016/j.corsci.2020.109005.

[79] Z. Liu and G. Welsch. "Literature Survey on Diffusivities of Oxygen, Aluminum, and Vanadium in Alpha Titanium, Beta Titanium, and in Rutile". In: *Metallurgical Transactions A* 19.4 (1988), pp. 1121–1125. ISSN: 0360-2133, 1543-1940. DOI: 10.1007/BF02628396.

[80] M. Yan, W. Xu, M. S. Dargusch, H. P. Tang, M. Brandt, and M. Qian. "Review of Effect of Oxygen on Room Temperature Ductility of Titanium and Titanium Alloys". In: *Powder Metallurgy* 57.4 (2014), pp. 251–257. ISSN: 0032-5899, 1743-2901. DOI: 10.1179/1743290114Y.0000000108.

[81] M. Yan, M. Dargusch, T. Ebel, and M. Qian. "A Transmission Electron Microscopy and Three-Dimensional Atom Probe Study of the Oxygen-Induced Fine Microstructural Features in as-Sintered Ti–6Al–4V and Their Impacts on Ductility". In: *Acta Materialia* 68 (2014), pp. 196–206. ISSN: 13596454. DOI: 10.1016/j.actamat.2014.01.015.

[82] H. Miura, H. G. Kang, and Y. Itoh. "High Performance Titanium Alloy Compacts by Advanced Powder Processing Techniques". In: *Key Engineering Materials* 520 (2012), pp. 30–40. ISSN: 1662-9795. DOI: 10.4028/www.scientific.net/KEM.520.30.

[83] A. Kahveci and G. Welsch. "Effect of Oxygen on the Hardness and Alpha/Beta Phase Ratio of Ti6Al4V Alloy". In: *Scripta Metallurgica* 20.9 (1986), pp. 1287–1290. ISSN: 00369748. DOI: 10.1016/0036-9748(86)90050-5.

[84] W. L. Finlay and J. A. Snyder. "Effects of Three Interstitial Solutes (Nitrogen, Oxygen, and Carbon) on the Mechanical Properties of High-Purity, Alpha Titanium". In: *JOM* 2.2 (1950), pp. 277–286. ISSN: 1047-4838, 1543-1851. DOI: 10.1007/BF03399001.

[85] G. Welsch, R. Boyer, and E. W. Collings, eds. *Materials Properties Handbook: Titanium Alloys*. Materials Park, OH: ASM International, 1994. ISBN: 978-0-87170-481-8.

[86] W. Xu, E. Lui, A. Pateras, M. Qian, and M. Brandt. "In Situ Tailoring Microstructure in Additively Manufactured Ti-6Al-4V for Superior Mechanical Performance". In: *Acta Materialia* 125 (2017), pp. 390–400. ISSN: 13596454. DOI: 10.1016/j.actamat.2016.12.027.

[87] Y. Ren, X. Lin, X. Fu, H. Tan, J. Chen, and W. Huang. "Microstructure and Deformation Behavior of Ti-6Al-4V Alloy by High-Power Laser Solid Forming". In: *Acta Materialia* 132 (2017), pp. 82–95. ISSN: 13596454. DOI: 10.1016/j.actamat.2017.04.026.

[88] L. Emanuelli, A. Molinari, L. Facchini, E. Sbettega, S. Carmignato, M. Bandini, and M. Benedetti. "Effect of Heat Treatment Temperature and Turning Residual Stresses on the Plain and Notch Fatigue Strength of Ti-6Al-4V Additively Manufactured via Laser Powder Bed Fusion". In: *International Journal of Fatigue* 162 (2022), p. 107009. ISSN: 01421123. DOI: 10.1016/j.ijfatigue.2022.107009.

[89] C. Buirette, J. Huez, N. Gey, A. Vassel, and E. Andrieu. "Study of Crack Propagation Mechanisms during Charpy Impact Toughness Tests on Both Equiaxed and Lamellar Microstructures of Ti–6Al–4V Titanium Alloy". In: *Materials Science and Engineering: A* 618 (2014), pp. 546–557. ISSN: 09215093. DOI: 10.1016/j.msea.2014.09.048.

[90] L. Lei, Y. Zhao, Q. Zhao, C. Wu, S. Huang, W. Jia, and W. Zeng. "Impact Toughness and Deformation Modes of Ti–6Al–4V Alloy with Different Microstructures". In: *Materials Science and Engineering: A* 801 (2021), p. 140411. ISSN: 09215093. DOI: 10.1016/j.msea.2020.140411.

[91] T. Mohandas, D. Banerjee, and V. Kutumba Rao. "Observations on Impact Toughness of Electron Beam Welds of an $A+\beta$ Titanium Alloy". In: *Materials Science and Engineering: A* 254.1-2 (1998), pp. 147–154. ISSN: 09215093. DOI: 10.1016/S0921-5093(98)00697-2.

[92] J.-Y. Buffiere, E. Maire, J. Adrien, J.-P. Masse, and E. Boller. "In Situ Experiments with X Ray Tomography: An Attractive Tool for Experimental Mechanics". In: *Experimental Mechanics* 50.3 (2010), pp. 289–305. ISSN: 0014-4851, 1741-2765. DOI: 10.1007/s11340-010-9333-7.